

# Studying Biofilm Development with Widefield Fluorescence Microscopy

Ben Wilson, supervised by Somenath Bakshi

June 4, 2022

Rather than floating freely, nearly all bacterial cells on Earth live on surfaces in the form of biofilms. In these large, often multispecies communities, cells are protected from their environment and are extremely hard to remove from the surfaces they are attached to. Biofilms are responsible for most of the world's persistent infections, interfere with industrial pipelines, and exacerbate the spread of multiple drug resistance. They also have potential to be exploited in applications ranging from energy generation to bioremediation efforts.

Therefore, there is a strong drive in the research community to understand biofilms' highly complicated structure and development. Numerous characterisation techniques exist, with valuable characteristics including speed, non-invasiveness (and therefore the ability to monitor biofilm development over time), ability to monitor large (mature) biofilms, fluorescent signal measurement capability (so that fluorescent markers and gene expression can be monitored), and ability to characterise individual cells within a biofilm rather than the bulk community as whole. Unfortunately, no technique exists which combines all of these strengths. The best option is often confocal scanning laser microscopy (CLSM), which allows 3D reconstruction of a biofilm in either brightfield or fluorescence channels. However, CLSM has two key limitations: scanning is extremely slow for anything but the smallest biofilms, and only gets slower if single-cell resolution is required, and detection fluorescent emission light only penetrates a small distance into a biofilm ( $\sim 40\mu\text{m}$ , depending on the fluorophore and imaging setup), limiting the size of biofilms that can be studied in full 3D.

In this project, 2D widefield fluorescence microscopy is applied to the characterisation of biofilms. The main accomplishments of the report include:

- **Development and optimisation of an imaging platform for non-invasive time-lapse imaging of biofilms.** The method developed involves imaging of a biofilm through agar medium upon which it grows. A number of practical problems with sample preparation are solved and protocol optimisations are made.
- **Development of a protocol and processing pipeline for estimation of biofilm volume from 2D fluorescence measurements.** In this protocol, microscope images are acquired of a strain of *E. Coli* that constitutively expresses yellow fluorescent protein (YFP). Extensive image processing corrects for various characterised components of microscope background noise, and overall received intensity is compared to that of single cells in order to estimate biofilm volume.

- **Development of an orthogonal assay to investigate the accuracy of this technique.** An assay is developed in which biofilms are disaggregated and fixed to agar for high-resolution fluorescence imaging. This is used to calculate the cell count within the biofilm, providing an orthogonal measurement for validation of intensity-based estimation. It is also used to characterise cell morphology and fluorescence intensity distributions within the biofilm, further investigating the validity of assumptions behind the method.
- **Investigation of scattering and absorption effects on measurements, and comparison to CLSM.** Monte-Carlo based optical simulations are developed to demonstrate the strengths of widefield fluorescence microscopy for biofilm characterisation relative to CLSM. It is found that widefield is significantly less susceptible to scattering effects within the biofilm, which is hypothesised to be the cause of CLSM depth penetration issues.

Overall, tools and methodologies were developed for non-invasive fluorescent microscopy studies on biofilms, which can be built on further in the future to investigate the development of biofilms using time-lapse experiments and disaggregation-based single-cell characterisation.

# Contents

<b>1</b>	<b>Introduction</b>	<b>1</b>
1.1	Biofilms . . . . .	1
1.2	Impact of biofilms . . . . .	2
1.3	Biofilm quantification methods . . . . .	3
1.3.1	Using widefield microscopy for biofilms . . . . .	4
1.4	Project objectives . . . . .	4
1.5	Previous relevant research . . . . .	5
<b>2</b>	<b>Methods &amp; Method Validation</b>	<b>6</b>
2.1	Protocol for colony growth and imaging . . . . .	6
2.1.1	Imaging setup overview . . . . .	6
2.1.2	Avoiding agar dehydration . . . . .	7
2.1.3	Ensuring flatness of agar to maximise image quality . . . . .	7
2.1.4	Imaging acquisition for TRI . . . . .	9
2.2	Practical methods to assess widefield characterisation accuracy . . . . .	10
2.2.1	Is cell fluorescence uniform within a biofilm? . . . . .	10
2.2.2	Fluorescence imaging of disaggregated cells . . . . .	12
2.2.3	Assessing the accuracy of the DFA counting method . . . . .	13
2.3	Image processing . . . . .	13
2.3.1	Image processing steps for TRI . . . . .	14
2.3.2	Image processing steps for DFA . . . . .	15
2.4	Monte Carlo optical simulations . . . . .	18
2.4.1	Penetration problems in CLSM . . . . .	18
2.4.2	Overview and limitations of Monte Carlo simulation . . . . .	19
<b>3</b>	<b>Results</b>	<b>21</b>
3.1	Accuracy of DFA counts . . . . .	21
3.2	Cell intensity and area distributions from DFA . . . . .	22
3.3	Biofilm volume from TRI vs control measurements . . . . .	22
3.4	Results of optical simulations . . . . .	22
<b>4</b>	<b>Discussion</b>	<b>25</b>
4.1	Accuracy of DFA counts . . . . .	25
4.2	Cell intensity and area distributions from DFA . . . . .	25
4.3	Biofilm volume from TRI vs control measurements . . . . .	26
4.4	Results of optical simulations . . . . .	26
<b>5</b>	<b>Conclusions &amp; Future Directions</b>	<b>27</b>
<b>6</b>	<b>Acknowledgements</b>	<b>28</b>
<b>A</b>	<b>Overview of biofilm characterisation techniques [40]</b>	<b>29</b>
<b>B</b>	<b>Optimisation details of agar preparation</b>	<b>30</b>
<b>C</b>	<b>O<sub>2</sub> depletion calculation parameters</b>	<b>31</b>

<b>D Optimisation details of DFA</b>	<b>31</b>
D.1 Fixation technique . . . . .	31
D.2 Method of disaggregation . . . . .	32
<b>E Details on microscope image intensity correction</b>	<b>35</b>
E.1 Dark signal . . . . .	35
E.2 Beam leakage . . . . .	36
E.3 Beam profile . . . . .	37
E.4 Image stitching correction . . . . .	38
E.5 Photobleaching considerations . . . . .	38
E.6 Image correction code . . . . .	39
<b>F Overview of fluorescence microscopy optics</b>	<b>40</b>
F.1 Widefield microscopy [50] . . . . .	40
F.2 Confocal Laser Scanning Microscopy [53] . . . . .	40
F.3 Other optical effects . . . . .	41
<b>G Optical Monte Carlo simulation procedure [39]</b>	<b>42</b>
<b>H Risk Assessment retrospective</b>	<b>44</b>

# 1 Introduction

This project aims to investigate protocols for imaging bacterial biofilms using fluorescence microscopy, determining the conditions under which these widefield techniques may be superior to traditional methods for characterising their growth and size.

## 1.1 Biofilms

Bacterial biofilms are surface-bound, three-dimensional communities of bacteria embedded in a self-produced extracellular matrix. Capable of withstanding much harsher conditions than constituent cells in their free-floating planktonic form, biofilms are highly abundant, accounting for ~80% of all bacterial cells or over half of all cells on earth [3].

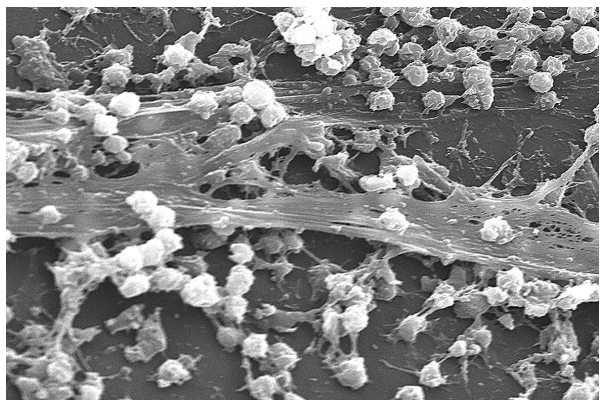
Communities are instigated by reversible attachment of planktonic cells onto a surface, which triggers active irreversible attachment on the timescale of minutes [4]. A number of dedicated surface proteins have been implicated in encouraging this contact, as well as facilitating locomotion and aggregation of cells across the surface [5]. Both biotic and abiotic interfaces are susceptible to colonisation; in fact, almost any solid or liquid boundary is sufficient [6].

In the newly-formed microcolonies, cells produce an extracellular polymeric substance (EPS) constituting mainly polysaccharides, but also a variety of proteins, DNAs and lipids [7]. This EPS acts as a structural ‘glue’ that holds embedded cells to each other and to the surface [8]. It also acts as a buffer, protecting cells from hostile external environments and mechanical forces: biofilms have been found in niches as hostile as acid mine runoff streams, and are highly resilient to antibiotics [9], [10].

As these communities grow, cells undergo significant alterations to their gene expression, shifting their behaviour to this new lifestyle and sometimes causing specialisation of sub-communities. Potentially highly complex shapes and behaviours are possible thanks to a combination of environmental stimuli and the quorum sensing (QS) of auto-inducing molecules, which allow cells to sense each other’s presence and regulate gene expression in response to population density changes [11]. Channel networks commonly form within the structure, resolving nutrient and waste diffusion limitations [12]. Beneficial effects of living in a multicellular communities are only amplified by the introduction of additional



(a) Biofilm (yellow) on Yellowstone Volcano. From [1].



(b) *Staphylococcus aureus* biofilm on an indwelling catheter. From [2].

**Figure 1:** Example images of biofilms.

mutualistic bacterial species, further increasing the complexity of most biofilms found in nature [13].

## 1.2 Impact of biofilms

### Medical implications

Bacterial biofilms form the basis of around 80% of persistent infections [10]. Infections of implanted medical devices such as heart valves, pacemakers and catheters commonly picked up in hospitals (estimated 1.7 million hospital acquired infections per year in the US) and are notoriously difficult to resolve due to biofilms' outstanding resilience [14]. In addition to EPS-related protection from immune cells and medical treatments, the large community allows for delegation of tasks (such as production of agents that combat antibiotics) to a subset of cells and population bet-hedging (for example, some 'persister' cells are able to reduce their metabolism, rendering many antibiotics ineffective) [15]. Moreover, exchange of antibiotic resistance plasmids is enhanced within the biofilm, encouraging proliferation of the global health concern of multiple drug resistance (MDR) [16].

### Industrial fouling

Biofilms induce significant economic costs by blocking and degrading industrial pipelines. In particular, biofouling of industrial and drinking water infrastructure is ubiquitous [17], and there is risk of food-borne diseases developing from biofilm development within food industry factories [18].

### Exploitation

There is interest in deploying biofilms within a number of fields. Industrial applications include food fermentation, biofertilizer, filtration, prevention of corrosion, wastewater treatment and within microbial fuel cells [19]. Additionally, it may be possible to exploit them for environmental repair or bioremediation, taking advantage the efficiency at which they absorb, immobilise, and degrade many environmental contaminants [20], [21]. They may even provide an energy source for the future [22]

### Consequences for the scientific community

Given the mentioned impact areas as well as a number of others, the economic significance of biofilms has been conservatively estimated to be in excess of \$5,000bn annually [23]. Much research therefore has been directed toward their characterisation. It is hoped that enhanced understanding of the development of biofilms will lead to new methods and new drugs to inhibit their formation [24], [25]. This understanding, however, relies on appropriate tools and techniques to track and visualise their world. Knowledge of total biomass is important in clinical and industrial tracking: for example, to determine the extent of infection or for process control of treating agents respectively, or to determine the extent of infection of retrieved implanted devices. Additionally, on a basic research and understanding level, it is crucial to be able to track the growth and behaviour of biofilms to a very high precision.

### 1.3 Biofilm quantification methods

A large range of techniques for characterising biofilms are employed in the literature and for industrial or medical assessment. A fundamental parameter is the total accumulation of biomass or, equivalently, volume (since density is near-constant). This answers the simple question, “How much biofilm is there?”, and is sufficient for a variety of industrial and medical assays. The question can be answered either by counting the number of cells, or by using some other physical technique to measure the full, combined biomass or volume. If a cell-counting method is used, ideally, the volume (or mass) for each cell should be available to give an accurate total volume (or mass). This volume distribution can itself be useful for the characterisation of biofilms.

Two useful extensions to bulk biofilm measurements exist: Shape measurement, and targeted fluorescence measurement. The latter refers to quantifying a particular type of molecule within a biofilm by a unique fluorescent signature or added tag, either using staining or genetic engineering. Both of these can provide significantly greater insight to the inner workings of biofilms and their emergent structure, principally in the research domain.

Measurements to obtain each of these parameters can be either destructive or non-

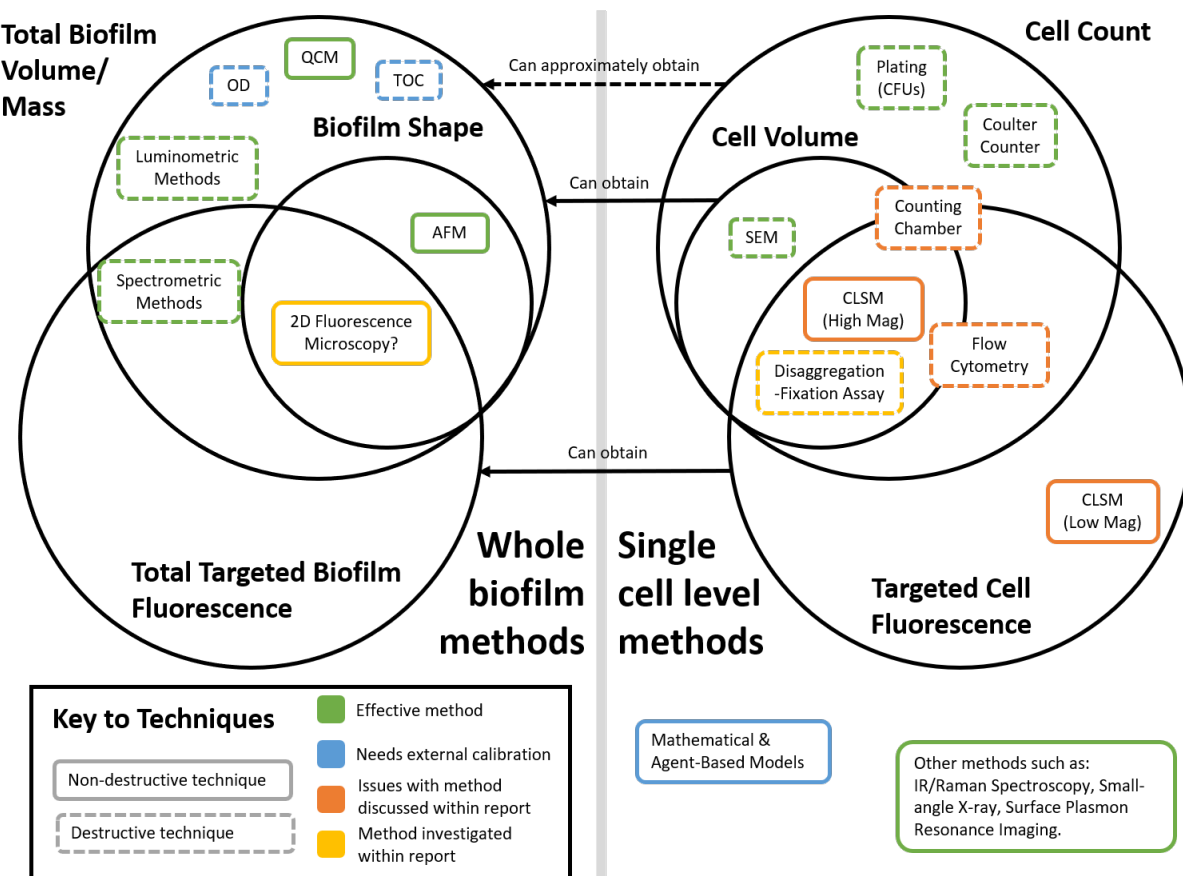


**Figure 2:** Illustration of characterisation methods available for quantification of biofilms, arranged in a Venn diagram-like structure. The left-hand side contains methods for one-shot measurements on an entire biofilm, while the right-hand side contains techniques for characterising cells *within* a biofilm. Where methods overlap the boundary between two or more sets, it is ambiguous or debatable which sets the technique qualifies for. “Targeted Fluorescence” refers to measurement of fluorescently-tagged molecules or dyes.

destructive. Non-destructive methods are more powerful, as they facilitate the ability to take time-lapse measurements - i.e., repeated measurement of the same colony as it matures. This is crucial to the understanding of biofilm development and maturation, which has particular application in the development of anti-biofilm agents that can disrupt their formation.

More powerful techniques exist that can take these abilities back down to the single-cell level, generally at the cost of comparable increases in complexity and effort. Non-invasive methods are again superior, especially if the locations of cells within the biofilm can be obtained alongside shape or fluorescence data. The ‘holy grail’ of biofilm characterisation is a non-invasive, targeted-fluorescence-capable, location-determining technique that can be applied to biofilms of any size. Although confocal laser scanning microscopy (CLSM) comes close to achieving this, its power can mostly only be leveraged for small biofilms.

Figure 2 provides a visual overview of techniques, grouped by important capabilities. See Appendix 1 for more detail and a brief discussion of each method.

### 1.3.1 Using widefield microscopy for biofilms

A possible technique that has received little attention in the literature is 2D fluorescence microscopy. Almost every biology lab possesses such an instrument, and although the 2D nature of widefield microscopy makes full 3D reconstruction of a biofilm an inherently ill-posed problem, there is still plenty of information to be gleaned.

Simplistically, the imaging process can be thought of as capturing an axial projection of all fluorescent activity within a microscope’s depth of focus (this will be discussed in more detail later). This naturally leads to the idea of using projected intensities of a uniformly-fluorescing biofilm to recover changes in its relative thickness, extracted via intensity contours. Given the intensity and size of a single cell, this could also lead to estimates of cell counts within the colony, as well as the potential estimation of full metric 3D structure.

This technique may result in a fast and accessible method applicable even to very large and thick biofilms. Additionally, it is non-invasive, so could facilitate time-lapse monitoring if a genetically engineered cell strain is used to constitutively express fluorescent protein. The model organism used to test and develop methods is *E. Coli*.

## 1.4 Project objectives

Recovering the volume and shape of a biofilm from the proposed fluorescence measurements relies on the assumptions that (i) all parts of the biofilm are uniformly concentrated with fluorophores, and (ii) the amount of intensity recovered is also independent of position within the biofilm. These assumptions are by no means necessarily true: a defining feature of biofilms is enormous heterogeneity in chemical environments and constituent cells, and the imaging process is more complex than a simple 2D projection. The regions of validity of these assumptions should be investigated.

Therefore, the initial objectives for this project were as follows:

### A. Develop and optimise an imaging platform for non-invasive time-lapse imaging of biofilms.

A number of practical problems are inherent to attempting and validating time-lapse imaging of biofilms, including control of the agar surface, observation setup, and orthog-

onal methods to count the number of cells and investigate fluorescence behaviour within the biofilm. As part of this objective, a procedure called a disaggregation-fixation assay (DFA) was developed that enables single-cell fluorescence and shape characterisation of a disaggregated biofilm, by fixing a sample of the cells on agar and applying further 2D microscopy with image processing.

### **B. Quantify biofilm volume using widefield fluorescence imaging - Total Received Intensity (TRI) method.**

The principal goal of this work was to develop a technique to estimate total biofilm volume from fluorescent intensity measurements, and assessing its accuracy and limitations.

### **C. Quantify biofilm shape and validate with CLSM measurements.**

The utility of widefield fluorescence microscopy for biofilms could be significantly enhanced if intensity contours can be used to recover their shape (for example, to validate development models). Therefore, a secondary aim was to investigate the feasibility of such a technique.

### **D. Non-invasive time-lapse imaging of biofilms**

A key potential advantage of this technique is the ability to non-invasively track the development of biofilms up to a very large size. It was not possible to carry out a time-lapse imaging series due to time constraints; however, all methods have been designed under the consideration that they should be applicable to this scenario.

## **1.5 Previous relevant research**

Some previous attempts have been made to leverage 2D microscopy data, both with fluorescent staining and without.

**Brightfield Attenuation (2018).** In [26], a biofilm is illuminated in brightfield and the resulting gray level is measured versus position to determine thickness and volume. The method was found to correlate well to cryo-sectioned fluorescence validation data, but its dynamic range is limited to between 3 and 120 cells, and little detail or attention is paid to the method's precise optics and limitations. Additionally, calibration is required for each imaging scenario, requiring access to cryo-sectioning techniques.

**2D Fluorescence (2020).** A 2D fluorescence approach is applied in [27] to estimate biofilm thickness versus position, relative to single-cell intensity readings. This is very similar in principle to the work presented here, with the exception of using fluorescent staining. However, the paper focusses on high-level description of a processing algorithm, with minimal substantiation of measurements and no consideration of error sources, putting its validity into question.

## 2 Methods & Method Validation

This section will detail and justify a protocol for applying both volume estimation (via TRI) and shape estimation to colonies of *E. Coli*, as well as the methods of validation steps taken. Next, an optical simulation procedure will be described to understand the mechanisms that affect the viability of widefield fluorescence versus CLSM. A strain harbouring a p-rpSL-mVenus construct and motA deletion was chosen (designated SB6). Practically, this means that the strain is immobilised due to a flagellum gene being knocked out, and the yellow fluorescent protein mVenus (YFP) will fluoresce when excited at around 514nm.

### 2.1 Protocol for colony growth and imaging

The traditional growth medium for *E. Coli* of agar infused with Lysogeny Broth (LB) was used. In order to keep techniques as generally applicable and non-invasive as possible, a setup was devised to image colonies directly on agar. This section will describe how colonies were prepared and imaged.

#### 2.1.1 Imaging setup overview

The microscope used within the Synthetic Biology lab is an inverted Nikon Ti2 Eclipse. The inverted setup means that in order to directly image the agar surface, the colony would have to face upside-down over the objective lens. This was undesirable due to the potential of condensation forming on the lens. Therefore, the choice was instead made to image through agar. 15ml of 1.5% agar was poured per plate (inner diameter 8.8mm), resulting in a thickness of 2.5mm, in addition to the thickness of the plate bottom. This required an extra-long working distance (ELWD) objective. The lab possessed one such objective at 40x magnification (see Table 1). For brightfield images, Phase-Contrast (PC) imaging was used [29].

It was possible to image colonies directly through the bottom surface of petri dish. Individual cells on the agar surface could be seen, but only at long exposures ( $\sim 1s$ ), and scattering caused a blurring effect. The poor optical interface provided by the plastic meant that cutting out a small chunk of agar and mounting it on a glass cover slide was preferable (Fig 21).

*Modification for time-lapse imaging:* It is possible to obtain glass-bottomed petri dishes, allowing the quality of Fig 4b without disruption to the colony.

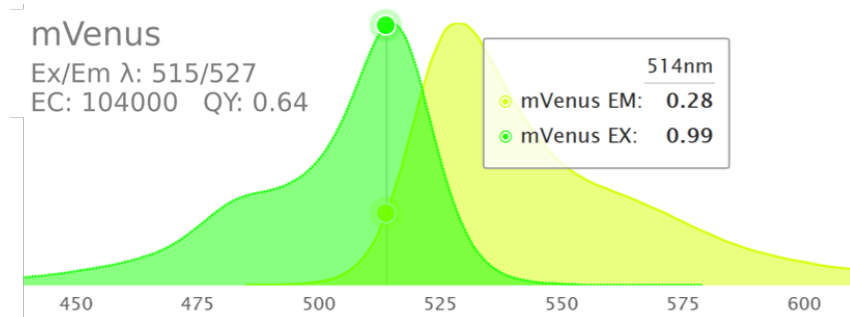
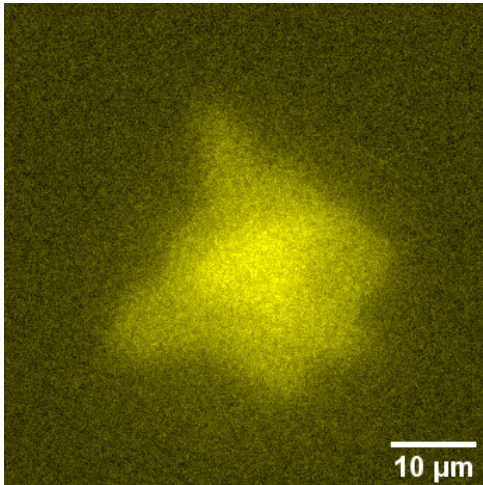
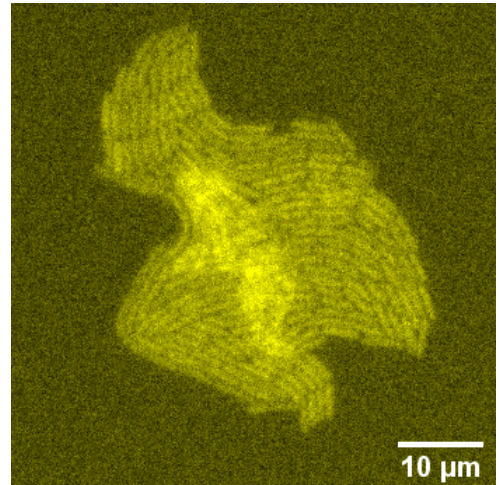


**Figure 3:** YFP (mVenus) excitation and emission spectra. Taken from [28].



(a) A small two-layer colony imaged in YFP through a plate.



(b) A different two-layer colony imaged in YFP through a cover slide.

**Figure 4:** Visual comparison of fluorescence images taken through a plate vs a cover slide. These images have been corrected as per Section 2.3.1. Both were imaged with the same parameters (5s exposure, 100% beam power).

### 2.1.2 Avoiding agar dehydration

Gradual dehydration of the agar in a typical environment causes the focal plane to slowly shift relative to the colony. This causes problems for time-lapse imaging. It was found from CLSM investigations that the shrinking rate of a cut-out agar chunk of given size is linear and highly predictable (at around 0.3% or  $7.5\mu\text{m}$  per minute for a chunk of  $\approx 8 \times 16 \times 2.5\text{mm}$  agar), with smaller chunks shrinking faster than larger.

In this work, chunks of between  $5 \times 5\text{mm}$  and  $10 \times 10\text{mm}$  were used, and imaging was fast enough that shrinkage was negligible compared to the objective's depth of field<sup>1</sup>.

*Modification for time-lapse imaging:* Mitigation of shrinkage is required. One option is humidity control in the imaging environment; another is the use of custom-made imaging devices with liquid channels in contact with the agar to provide nourishment.

### 2.1.3 Ensuring flatness of agar to maximise image quality

If the agar surface itself is not flat on the large scale, the plane of the colony may be angled with respect to the imaging plane, which was found to give significant loss of focus

<sup>1</sup>~1s for most colonies, and up to ~2min for the largest colonies, with height ~100-1000μm, so that drifts in focus were negligible relative to their dimensions

Lens	Numerical Aperture	Working Distance	DOF at 530 nm	Full Name
40x	0.95	250 μm	183 nm	Plan Apo λ 40x Ph2 DM
40x ELWD	0.60	3600 μm	1.18 μm	S Plan Fluor ELWD 40x Ph2 ADM
20x	0.75	1000 μm	623 nm	Plan Apo λ 20x Ph2 DM

**Table 1:** Lenses used in microscope.

for larger colonies. Small-scale imperfections, meanwhile, can cause imaging artefacts (see Fig 5). Standard plate preparation leads to large-scale wrinkling and warping of agar, and standard inoculation methods using either a plastic spreader or glass beads result in small-scale damage. Alternative methods were therefore devised, following experimentation that is discussed in Appendix B. The results of this investigation resulted in the following protocols:

### Procedure 1: Agar Treatment

1. Heat LB agar (1.5%) in a temperature-controlled oven to 65°C.
2. Pipette 15ml onto an agar plate.
3. Immediately place in incubator at 37°C and leave for 15 mins<sup>2</sup>.
4. Leave plate at room temperature with lid on for at least 30 mins.

### Procedure 2: Plate Inoculation

1. Leave agar plates in flow hood with lids off for 15 minutes to dehydrate slightly.
2. Drop 500µl of cell suspension at the desired dilution onto the surface, spreading droplets uniformly.
3. Shake gently in orthogonal horizontal directions to coat the entire surface.
4. Leave to fully soak/evaporate for a further 15 minutes before placing in the incubator.

This inoculation method results in a uniform coverage without allowing excess surface liquid to remain and disrupt colony formation. It is important to ensure the plates dry on a level surface. The source of cells was an overnight LB culture in stationary phase (SP), grown from a single colony of SB6. It was determined experimentally that the dilution range required to obtain between 200 and 10 colonies was respectively  $2 \times 10^7$  to  $4 \times 10^8$ .

---

<sup>2</sup>It is important to ensure that the incubator is level for the cooling process.

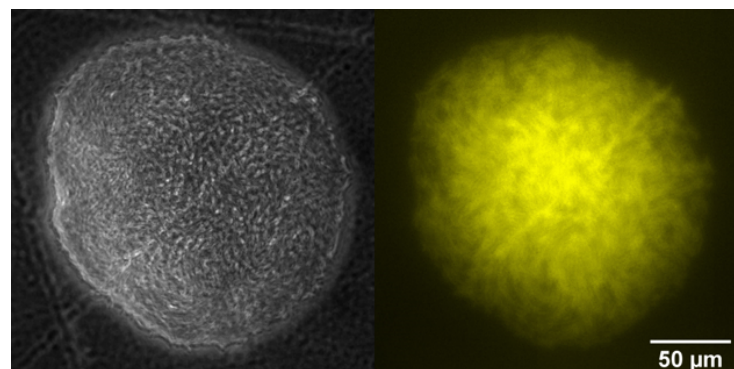


**Figure 5:** Micro-scale damage can cause imaging artefacts (the straight lines in these images).

#### 2.1.4 Imaging acquisition for TRI

Once an agar plate was prepared and colonies grown to an appropriate size, colony image was performed as follows:

#### Procedure 3: Colony Imaging

1. Focus to the base of the colony using a Phase Contrast channel and a 40x ELWD objective.
2. If the colony is larger than  $374.4\mu\text{m}$ , i.e. a single field of view (FOV) at 40x, set up an imaging schedule to capture a grid over the colony. The grid was set travel 0.2mm in between FOVs, resulting in a 47% overlap.
3. Image in PC to test the grid, then image in both YFP and PC, with 100% beam intensity and a YFP exposure as low as possible to provide a good signal-to-noise ratio while minimising photobleaching and cytotoxicity. 5s was used for the smallest colonies ( $d < 100\mu\text{m}$ ), 100ms for intermediate sizes ( $100\mu\text{m} \leq d < 1\text{mm}$ ), and 10ms for very large colonies ( $d \geq 1\text{mm}$ ).

An LED excitation beam at 514nm was used, with a dichroic filter passband of  $514\pm15\text{nm}$  appropriate for mVenus (Fig 3). “Ultra-low Noise” mode was enabled in acquisition controls, and the beam shutter was configured to be closed during microscope travel. For each agar plate, it was also important to estimate the intensity of a single cell, as well as the background beam profile<sup>3</sup>. Consequently, a set of images were also captured of empty agar (focused at the surface) and of individual cells. The latter images were obtained by dropping  $5\mu\text{l}$  of a 1:100 dilution from stationary phase and allowing it to soak into the agar.

---

<sup>3</sup>These settings and requirements will be discussed further in Section 2.3 on image correction.

## 2.2 Practical methods to assess widefield characterisation accuracy

The main points to investigate about the application of widefield fluorescence microscopy are as follows:

- **Uniform Fluorescence.** Do cells fluoresce near-uniformly within biofilms?
- **Overall TRI Accuracy.** Do estimated volumes from the TRI method align with true volumes? If not, how and where do they deviate?
- **Microscope Optics.** How much does the received intensity deviate from a simplified axial projection of fluorophore density? How does this depend on colony size?

Methods used to investigate the first two questions are described in this section. Monte Carlo methods to study microscope optics are described in Section G.

### 2.2.1 Is cell fluorescence uniform within a biofilm?

The potential sources of variability in cell fluorescence include:

1. **Concentration differences.** This may be due to changes in gene expression, or changes in dilution rate due to growth. Changes in expression could be due to a variety of factors, such as nutrient availability, or other biofilm-specific gene regulatory network shifts due to (for instance) quorum sensing.
2. **Fluorescence differences.** Even given the same YFP concentration, fluorescence is not necessarily fixed. GFP-derived proteins require oxygen to mature into a fluorescent state, and undergo conformational changes under pH changes that alter fluorescence activity.
3. **Concentration Stochasticity.** At the cellular level, there is intrinsic stochasticity in protein counts due to random molecular interactions and diffusion and small copy numbers that can deviate significantly from population averages. This is unlikely to cause significant error if spatially independent, as long as the cell count is sufficiently large.

Previous work by the Bakshi lab has provided evidence that the promoter for the 30S ribosomal subunit, p-rpSL, possesses highly robust expression throughout the bulk culture growth curve by using a microfluidic device known as a mother machine [30]<sup>4</sup>. This was hypothesised to be due to the fact that *E. Coli*'s growth rate is limited by ribosome count, and so a fixed proportion of its mass will always be composed of ribosomes. As a result, proteins sharing a promoter will be expressed in proportion to cell mass (or volume). However, this fact does not necessarily carry over to a biofilm environment.

---

<sup>4</sup>An attempt was made to recreate this experiment, with the intention of varying environment parameters such as oxygen concentration to characterise robustness. However, issues with loading the device meant that no results were obtained. Afterwards, the focus of experiments shifted towards *in situ* assays.

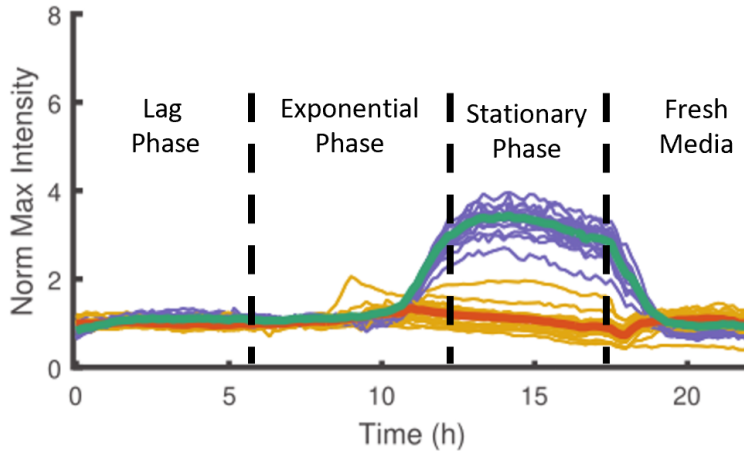


**Figure 6:** Expression dynamics of green fluorescent protein promoted by p-rpSL (orange/yellow) in individual cells within a mother machine over the course of a growth curve, compared to an alternative promoter expressing RFP, p-RNAI (green/purple). Note that p-rpSL's population average is near-constant. Taken from [30].

Back-of-the-envelope calculations indicate that oxygen depletion is unlikely to occur until at least 60-70 $\mu\text{m}$  in a typical colony of *E. coli*<sup>5</sup>. It is expected that pH changes are themselves a result of anaerobic conditions. Observed variation of pH with depth in colonies of *B. cereus* implies that for small biofilms (height  $\sim 10\mu\text{m}$ ), gradients are indeed negligible [32]. For larger biofilms, the impact of oxygen depletion may result in reduced fluorescence. Alternative signalling molecules that are insensitive to oxygen such as Flavin-binding fluorescent proteins [33] may assist in regimes where oxygen penetration becomes a problem.

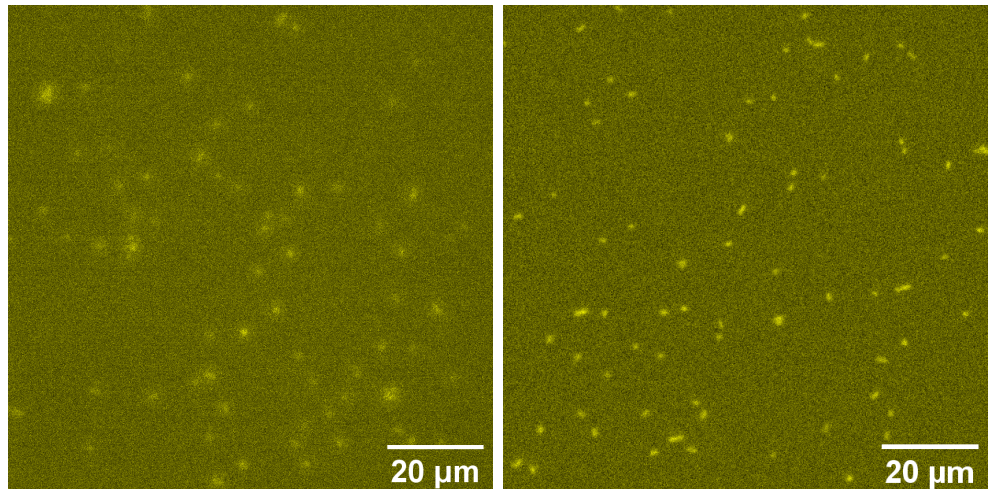
Ideally, a method should be available to verify fluorescence alongside cell volume *in situ* to investigate all of these phenomena.

Out of the techniques described in Appendix A, those relevant include CLSM, flow cytometry, and cryosectioning. Flow cytometry was not possible<sup>6</sup> - although regardless of availability, it has previously been found by the Bakshi lab that although fluorescence quantification with these instruments is accurate, for *E. Coli*, backscatter-derived size measurements are obfuscated by a large amount of noise due to the dependence of signal on the random orientations of cells passing through the device. Cryosectioning is a slow process requiring expert training that was not easily available, so this was also rejected. CLSM was therefore used to obtain *in situ* fluorescence data. However, it was swiftly discovered that CLSM was also inappropriate in this context, due to penetration issues that will be discussed in section 2.4.1, in addition to its low sensitivity.

---

<sup>5</sup>Penetration depth  $d_0$  can be estimated by considering a flat slab of biofilm, and applying the reaction-diffusion equation with zero-order reaction kinetics. Then  $d_0 = \sqrt{2D_{O_2}S_p/k_{O_2}}$  where the volumetric  $O_2$  reaction rate  $k_{O_2} = \mu X/Y_{O_2/X}$ , obtained via bacterial growth dynamics [31]. Other parameters and their values are defined and sourced in Appendix C.

<sup>6</sup>A lab in Cambridge with a flow cytometer was reached out to, but were not willing to put bacteria through the machine (which they normally use for blood cells).



(a) SP cells in a counting chamber. (b) SP cells fixed on agar via DFA.

**Figure 7:** YFP images of the same cell suspension diluted from stationary phase in a Petroff-Hauser chamber and fixed on agar, taken with a 40x objective, 40ms exposure, and 100% beam power. Images corrected as in Section 2.3.

### 2.2.2 Fluorescence imaging of disaggregated cells

Imaging of a sample of cells from a disaggregated biofilm under a microscope provides an opportunity for fluorescence measurements accessible to most labs.

With this idea in mind, a Petroff-Hauser counting chamber was purchased [34], with the intent of using it not just for its standard function of cell enumeration, but also to take high-resolution microscopy images to quantify cells' shape and fluorescence. Unfortunately, the chamber had a depth of 20 $\mu\text{m}$  (and was the shallowest available option). While this limits the mobility of cells enough to count them, it is still large compared to the scale of a single *E. Coli* cell. This resulted in images that resolved cells poorly, most likely due to a combination of Brownian motion over the exposure time and varying axial positions outside of the objective's depth of focus. To avoid this issue, the disaggregation-fixation assay (DFA) was developed as a method of fixing a sample of biofilm cells on agar, in order to allow much more precise imaging of cells' shape and fluorescence.

#### Procedure 4: Disaggregation-Fixation Assay

1. Prepare a plate of flat M9 agar (see Appendix B for notes on this).
2. Cut out a chunk of agar with a single colony using a sterile knife and place it in a cuvette, avoiding agar damage.
3. Wash & immerse in 200-1000 $\mu\text{l}$  of M9 media.
4. Vortex at 10,000rpm for up to 1 minute.
5. Pipette 3 droplets of 1 $\mu\text{l}$  each onto a flat 15ml plate of M9 agar.
6. Wait for media to soak into agar then cut out a chunk containing the droplets using a sterile knife, avoiding agar damage.
7. Flip the agar upside-down onto a microscope slide.

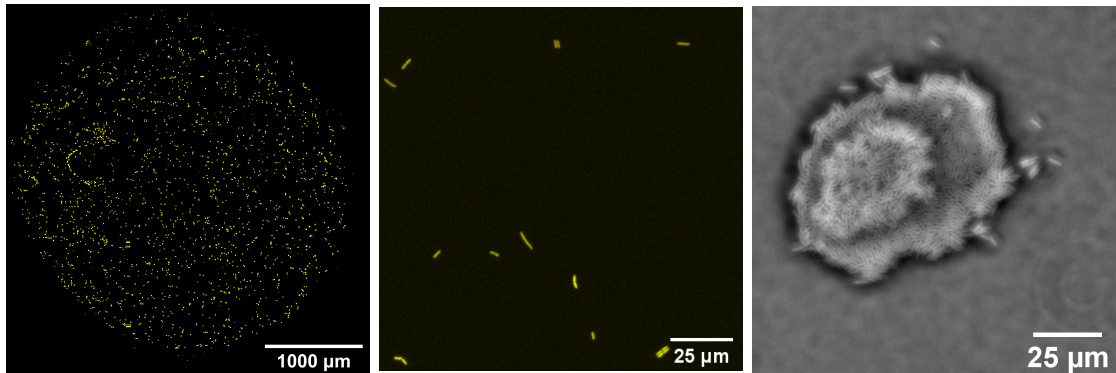
8. Image the full area of the droplet at 20x magnification for cell counting, or at 40x for full intensity and shape characterisation.

Note that this does not recover any spatial structure of changes in fluorescence. Therefore, it is still possible that shape estimation can be affected by, for example, a dimmer portion in the core of a biofilm.

### 2.2.3 Assessing the accuracy of the DFA counting method

To assess the accuracy of cell counting with the DFA, a serial dilution was performed on a SP culture with dilution ratios  $10^5$ ,  $5 \times 10^4$ ,  $2 \times 10^4$ ,  $10^4$ , ...,  $10^2$ .<sup>7</sup> For each dilution, three 1 $\mu$ l droplets were imaged. The droplet diameters were measured and found to be  $3300 \pm 155 \mu\text{m}$  with no correlation to cell concentration ( $r^2 = 0.015$ ), requiring a 6x6 grid of FOVs at 20x magnification to reliably capture. For very small colonies, there are not enough cells to be countable by microscope imaging - this was found to be the case below a colony diameter of  $\sim 100 \mu\text{m}$ . Thankfully, in these cases, layers of cells in the colony can be clearly differentiated using phase contrast imaging (Fig 8c). Measuring areas of each layer provides an alternative orthogonal technique for determining volume (using a nominal cell height of 1 $\mu\text{m}$  to measure heights).

A large amount of data is generated by this process due to the 36 FOVs, each containing  $2304 \times 2304$  pixels with bit depth 16 - resulting in 364 megabytes per assay. The analysis of this data is the subject of the next section.



(a) Full footprint of droplet. (b) Zoomed-in section of (a). (c) Small colony PC image.

**Figure 8:** Representative image outputs of the DFA counting method (cells from a disaggregated colony). In (a), the image has been max-pooled in 4x4 cells then thresholded to make visualisation possible with the large pixel count. (c) shows an example of a small colony whose volume can be quantified by measuring layer areas. (a) and (b) have been corrected and stitched as described in the next section.

## 2.3 Image processing

Careful quantification of fluorescence intensities is required to provide useful outputs from the techniques described in this report. Often, imaging operated close to the microscope's

---

<sup>7</sup>This series ended at 100 $\times$  dilution because it was assumed that by this concentration, it would become difficult to count cells due to the large number of aggregates, and also that the droplet precision may be reduced due to altered mechanical properties of the suspension.

noise floor, due to single-cell analysis and acquisition through relatively thick layers of agar. Therefore, considerable attention was paid to imaging artefacts and background characteristics of the microscope.

The following components all contribute, and have different relationships to the exposure time  $t$  and beam power percentage  $p$ :

1. **Dark signal.** This is signal present even when no illumination is present. It is the combination of a number of sources, grouped as *dark noise* from thermal effects and *read noise* in the circuitry, and has a constant offset at the limit of zero exposure due to amplification electronics [35].
2. **Beam leakage.** It was found that there is a constant-profile illumination pattern dependent on beam power and exposure time that appears even when nothing, or a matte black object, is being imaged. This is termed 'beam leakage'.
3. **Background fluorescence.** LB agar autofluoresces at the wavelengths used for YFP. M9 agar exhibits this behaviour to a milder extent.
4. **Nonuniform illumination profile.** Even an image of flat agar, after dark and leakage correction, has a characteristic intensity profile due to the inherent optics and variation in the excitation beam. The large field of view in the microscope used exacerbates this problem.
5. **Other Noise.** Ambient illumination or reflections and statistical variation in the number of incident photons on pixels (*photon noise*) lead to an additional statistical noise that has mean zero over time.
6. **Photobleaching & Phototoxicity.** Exposing cells and fluorescent proteins to the high-intensity excitation beam leads to decay in the fluorophores' activity and can be cytotoxic. Note that widefield is generally less sensitive to these problems than, for instance, CLSM, due to the lower beam intensities used. However, it becomes important when images must be stitched.

A thorough treatment of these effects is given in Appendix E.

### 2.3.1 Image processing steps for TRI

#### Procedure 5: TRI processing

1. As part of the correction process, images of regions of flat agar on the same plate that the colony is imaged on are required. A  $6 \times 6$  grid of these images is obtained, ideally with the same exposure and beam intensity as used for the colony.
2. For each frame, run image correction code using the corresponding background profiles to convert raw images to normalised, corrected intensities.
3. For single-FOV colonies: Trace around the colony, and obtain the integrated intensity of this region, using ImageJ [36]. Then, trace around a nearby region of background with similar size, and obtain the mean intensity of this, too. Multiply this mean by the area of the colony and subtract from its integrated intensity.

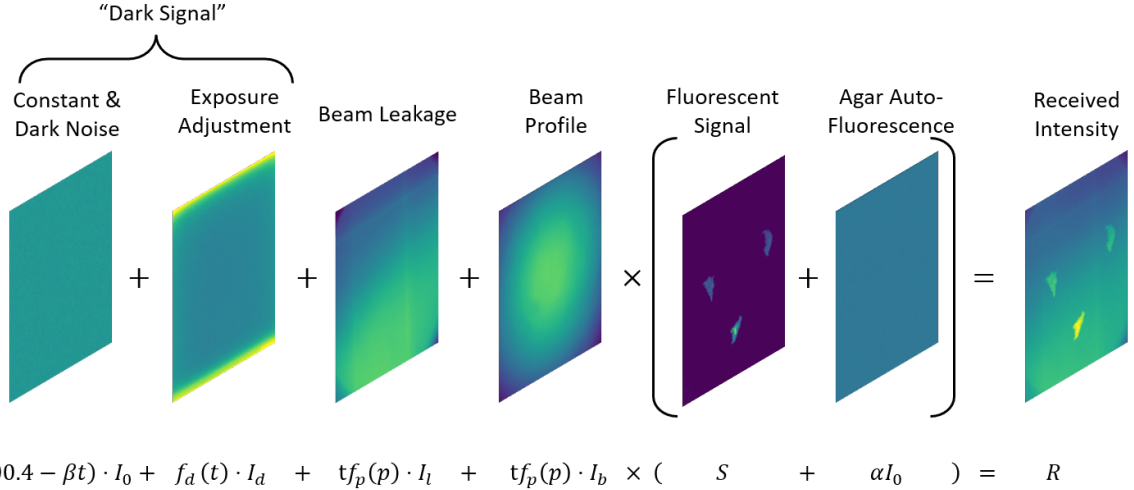


**Figure 9:** Diagram showing the components into which received intensity can be broken down. Additional noise is added due to ambient light and photon shot noise, not shown in the diagram. For description of the variables shown other than  $t$  and  $p$ , see Appendix E.

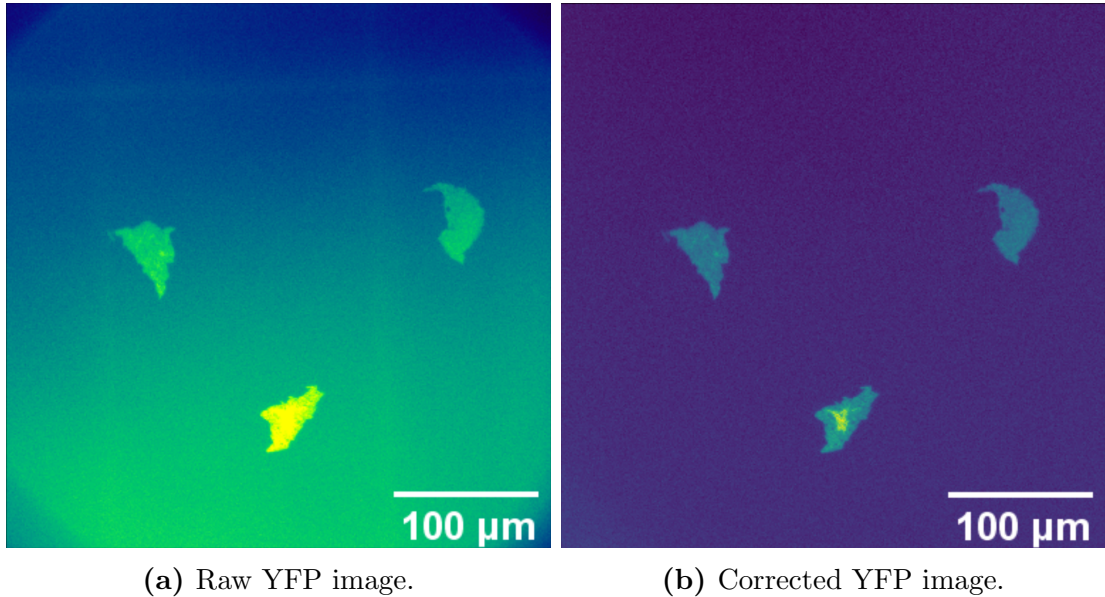
4. For colonies spanning 2-9 FOVs: Use only the first FOV for fluorescence quantification, as it is uncorrupted by photobleaching. This is sufficient to capture one-quarter of the colony, which is processed as for single-FOV colonies, but with the result multiplied by 4. Colony center locations and areas are obtained by stitching the PC-channel FOVs.
5. For colonies spanning 10 FOVs or more: It was found that for colonies spanning many FOVs, the overall fluorescent signal within the colony was attenuated by a factor approaching 0.832. Therefore, intensities were obtained after stitching the image by the same method as for single-FOV colonies, but with all values divided by this factor.
6. Once the mean, background-subtracted intensity has been obtained, this can be compared to the individual cells imaged on the same agar plate, and the intensity ratio used to find a mean height in cells. Assuming one cell has a height of  $1\mu\text{m}$ , volume can then be calculated in  $\mu\text{m}^3$ . For large colonies, SP cells were used. For small-colonies with a clear single-cell layer, the mean intensity of this layer was used.

Unfortunately, it was not possible to implement correction for photobleaching of neighbouring FOVs when capturing an image grid, hence the somewhat heuristic methods for multi-FOV colonies described in this procedure. See Appendix E for details.

### 2.3.2 Image processing steps for DFA

DFA presents further complications in data analysis. Accurate cell segmentation must be performed must be performed on a very large amount of data. This is important both for counting and for cell shape and fluorescence analysis.

The image correction process assists greatly with cell segmentation, resulting due to normalisation of the agar background intensity. After image stitching, a Gaussian blur can be applied, followed by thresholding above the (now reduced) background signal level.



(a) Raw YFP image.

(b) Corrected YFP image.

**Figure 10:** Example of the full image correction procedure on some small (1-2 layer) colonies. Imaging parameters were: 5s exposure, 100% beam power, 40x ELWD objective.

A morphological analysis can be applied on the resulting ‘blobs’ from this segmentation. The major flaw with this approach is that neighbouring cells and larger cell aggregates are treated as a single ‘blob’, potentially resulting in a significant underestimate of the cell count. This is exacerbated by the fact that, at 20x magnification, cells comprise only a small number of pixels, making it difficult to segment them into mutually separated contiguous blocks even with perfect knowledge of their shapes. One way to give additional flexibility to segmentation is to simply upscale the image by a factor of 2 (using bicubic interpolation).

For best performance, a machine learning (ML) based approach should ideally be used for cell segmentation. Implementation of an advanced ML architecture was out of the scope of the project; however, a plugin exists for ImageJ allowing interactive training of random forest-based ML model based on the Weka platform for Java [37]. This performed remarkably well with only a small number of training examples (Fig 11). Unfortunately, ML approaches tend to be extremely slow for large images - typical classification tasks use only 256x256 to 512x512 pixels.

To combine the strengths of ML with the speed of thresholding, the following procedure was used for DFA segmentation (both for 20x and 40x magnification images):

#### Procedure 6: DFA processing

1. Obtain an agar background profile by taking the per-pixel median across the images.
2. For each frame, use this profile to convert raw images to normalised, corrected intensities using the steps outlined previously.
3. Stitch the images.
4. Calculate the image median and inter-quartile range (IQR). The IQR provides a measure of variation that is more robust than standard deviation in the presence of very bright (outlier) cells on an otherwise dim background.

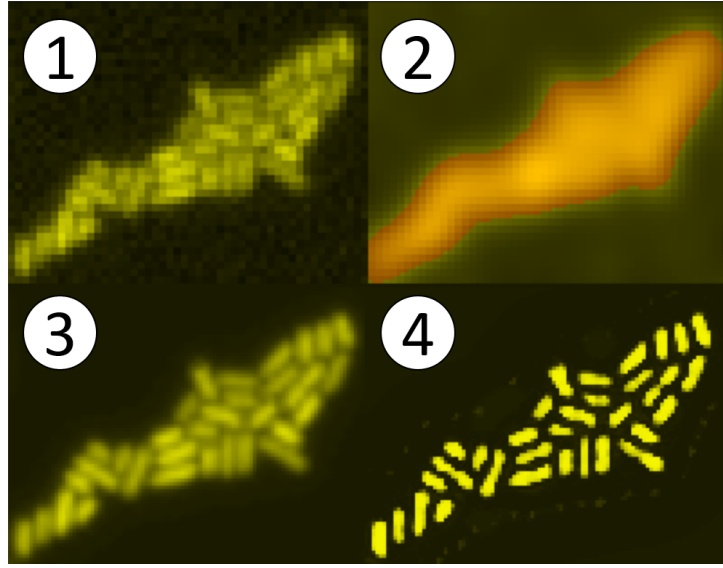


**Figure 11:** The segmentation process. The corrected image (1) is smoothed with a Gaussian blur of radius 2 which is thresholded to obtain a ‘blob’ mask so that it can be gathered into a dense image (image 2). It is separately upscaled by 2x (image 3), and ML is applied to this image to obtain class probabilities (image 4).

5. Apply a Gaussian blur with  $\sigma = 2\text{px}$  and use the previously calculated parameters to threshold the image at `median + 2*IQR`.
6. Using the `regionprops` method of `scikit-image` [38] with the thresholded image as a mask, analyse blob sizes. Filter out blobs less than  $0.1\mu\text{m}^2$  in area and morphologically dilate the remainder with a  $5\times 5\text{px}$  circular kernel. Bin blobs by their largest dimension (width or height). For each bin, create a dense grid of cells that fits within a  $512\times 512\text{px}$  frame (Fig 12). Assemble these into a z-stack. For ‘overflow’ blobs with dimensions greater than  $512\text{px}$ , create an additional overflow image.
7. Upscale the ‘dense’ images by a factor of 2 with bicubic interpolation.
8. Apply Weka segmentation to the z-stack to yield class probabilities. Threshold at 0.5 to obtain cell masks. Filter out blobs less than  $0.4\mu\text{m}^2$  in area and count.
9. If analysing the cell corresponding to a given labelled cell mask at 40x, morphologically dilate it with a  $3\times 3\text{px}$  circular kernel, since the segmentation mask is intentionally slightly smaller than the size of a cell so that cells can be easily separated.

Separate classifiers were trained for 20x and 40x magnifications. Some DFA images included a non-negligible proportion of out-of-focus cells. In these cases, a three-class classifier was trained with in-focus cells, background, and out-of-focus cells as the class targets. Pixels identified as out-of-focus cells were discounted if they were adjacent to pixels identified as in-focus cells to avoid double-counting. The performance of each classifier was manually checked on 150 randomly-selected outputs each, and performance was consistently strong (Table 2).

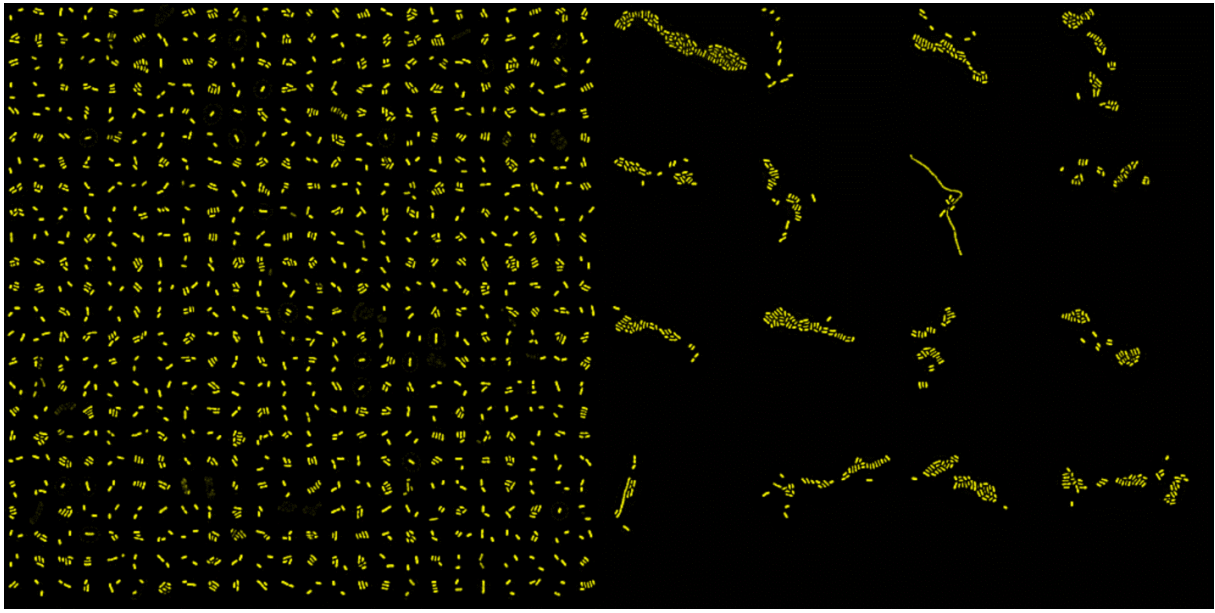


**Figure 12:** Dense cell images of two different bin sizes, obtained during Procedure 6.

Classifier	No. of aggregates	Of which correctly split	Overall count error	Naive count error
Binary, 20x	26	24	1.1%	34.7%
Binary, 40x	21	21	0.0%	19.3%
Trinary, 20x	14	10	4.0%	39.3%

**Table 2:** Classifier performance on 150 randomly selected blobs obtained from naive segmentation (i.e. simple thresholding).

## 2.4 Monte Carlo optical simulations

### 2.4.1 Penetration problems in CLSM

For three different colony sizes (627 $\mu\text{m}$ , 1.51mm and 2.27mm diameters), CLSM data was acquired in order to provide ground truth for colonies' precise shape. Colonies were imaged by cutting a chunk of agar, gluing its edges to a microscope slide, tapping this slide to settle the agar flat, then turning it upside down to be imaged from the biofilm's curved side. A 40x, 0.5 NA dry lens (HCX PL Fluotar x20/0.5 DRY) was used. Due to practical constraints with the location of the machines, it was not possible to image the same colony using both the Nikon widefield microscope and the CLSM, so these shapes were taken as representative for colonies of that particular diameter.

It was intended that ground truth could possibly be obtained for the fluorescence of a sample of individual cells *in situ*. It quickly became apparent, however, that only a relatively thin layer of fluorescent activity at the surface of the biofilm could be received by the CLSM. This was unlikely to be due to oxygen limitation, as it occurred on a scale of  $\sim$ 10-40 $\mu\text{m}$ .

This penetration issue has not been widely documented in the literature, but appears to be a fundamental limitation for scanning of biofilms, likely originating from either optical scattering or absorption. These factors, if limiting for CLSM, will be enlightening

to explore further. Therefore the imaging process for both CLSM and widefield in the presence of the two effects were explored via computational models. These models rely on a detailed understanding of microscope optics for CLSM and widefield; this topic is discussed in Appendix F.

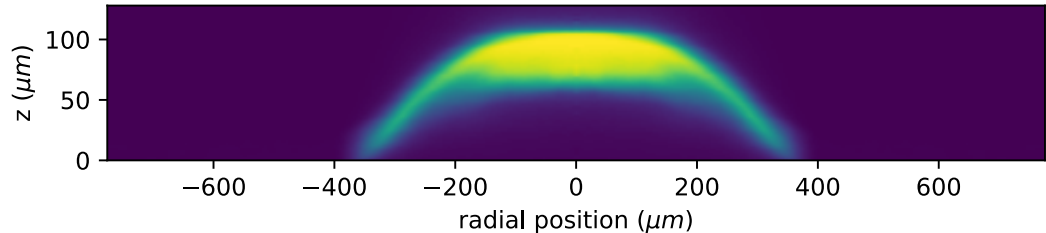


**Figure 13:** YFP fluorescence profile through a  $627\mu\text{m}$  diameter colony imaged using CLSM. This image was obtained by averaging a number of vertical sections rotated about the colony's centre. The biofilm was scanned from its top side. Note that only signal only penetrates up to a depth of  $\sim 40\mu\text{m}$  into the colony.

#### 2.4.2 Overview and limitations of Monte Carlo simulation

The only tractable form of model for complicated geometries such as biofilms when scattering or absorption are significant is a Monte Carlo method, tracking the propagation of individual photons and drawing path lengths until a scattering/absorption event and scattering directions from a parameterised random distributions [39]. Outside the media, photons are traced as rays and their image positions calculated accordingly. Only photons entering the objective lens within its acceptance angle are accepted. This form of simulation has the following limitations:

- Light is treated in discrete entities that do not interact; thus, interference phenomena are neglected.
- The true scattering orientation distribution is not known; a probability density function derived for a known case must be applied instead.
- Without knowledge of the detailed internal structure of a biofilm and how cell packing affects optics, the biofilm must be approximated as isotropic and homogeneous.

Note that the final point is likely not wholly accurate: in Fig 13, there appears to be deeper penetration at the centre of the colony than at its periphery. One possible explanation for this is that cells are verticalised in the centre of the biofilm, and therefore light is transmitted either due to cells directly light in an optical-fibre type matter of the fact that there will be fewer cell walls to interact with per unit length.

Two cases were considered: That of imaging a biofilm from the top using CLSM, with the same microscope parameters as used for the real CLSM data, and that of imaging from below in widefield using a CCD camera, analogous to the setup used in this report. Scattering within interposing agar was neglected for simplicity. The simulation procedure is discussed in more detail in Appendix G.

Biofilm geometry was approximated as a quadratic curve up to a flat top, and this profile was fit to the CLSM scans by considering the radius at which YFP signal disappears as a function of height, with a mean taken over radial lines swept at each height (Fig 14). The parameters were optimised with nonlinear minimisation. This form of fit was used for all three colonies to determine their volumes, and for simulations, different biofilm sizes were approximated by linearly scaling the 3D shape of the 627 $\mu\text{m}$ -diameter colony.

Scattering and absorption rates in simulation were calibrated in order to give penetration depths corresponding to those in Fig 13, i.e. in the approximate range 10-40  $\mu\text{m}$ .

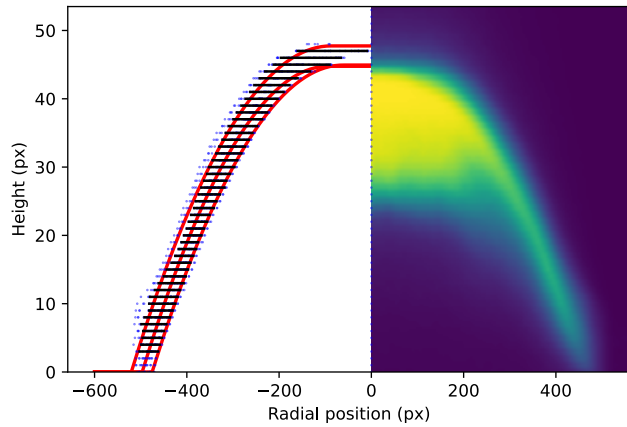


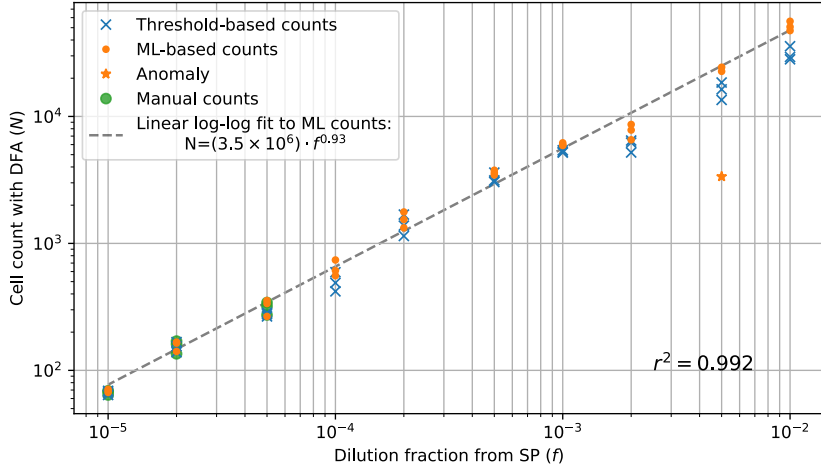
**Figure 14:** Illustration of best-fit parameterisations of the 627 $\mu\text{m}$ - diameter biofilm (red lines). Horizontal black lines and blue dots represent the variation of detected radius with angle. The three fits are to 5<sup>th</sup> percentile, median and 95<sup>th</sup> percentile radius estimates. The median was used going forward.

### 3 Results

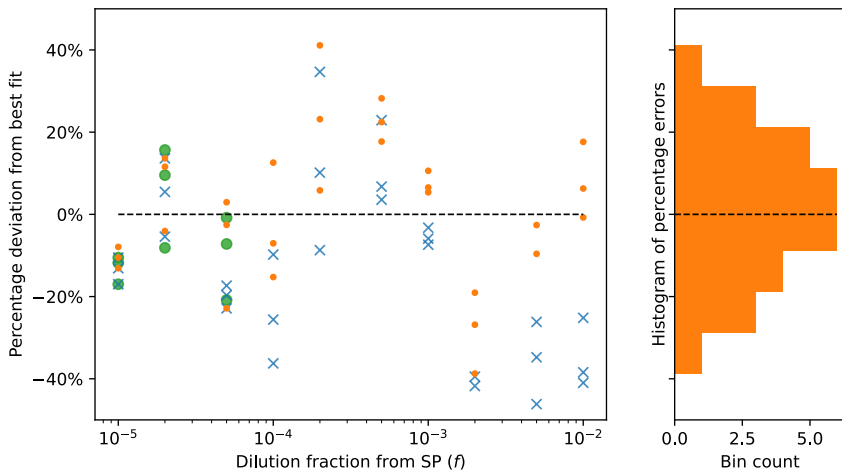
#### 3.1 Accuracy of DFA counts

The results of the serial dilution experiment used to assess DFA count accuracy are plotted in Fig 15, in addition to count based on a naive thresholding. For the three most dilute cultures, only a few tens to hundreds of cells were present in each  $1\mu\text{l}$  droplet, making it possible to perform manual counts as reference values.

A line of best fit was calculated for the logarithms of the cell counts  $N$  and dilution fractions  $f$ , resulting in the relation  $N = 3.5 \times 10^6 \cdot f^{0.93}$ , with an  $r^2$  value of 0.992. One count, evaluated at a dilution from SP of  $2 \times 10^2$ , was excluded from this fit as an outlier. Investigation of the source of this anomaly showed that a large proportion of the cells were very out of focus.



(a) DFA count calibration data.



(b) Percentage errors from linear best fit in log domain.

**Figure 15:** Calibration line for the DFA counting method.

### 3.2 Cell intensity and area distributions from DFA

Results are plotted as 2d histograms presented in Figure 16.

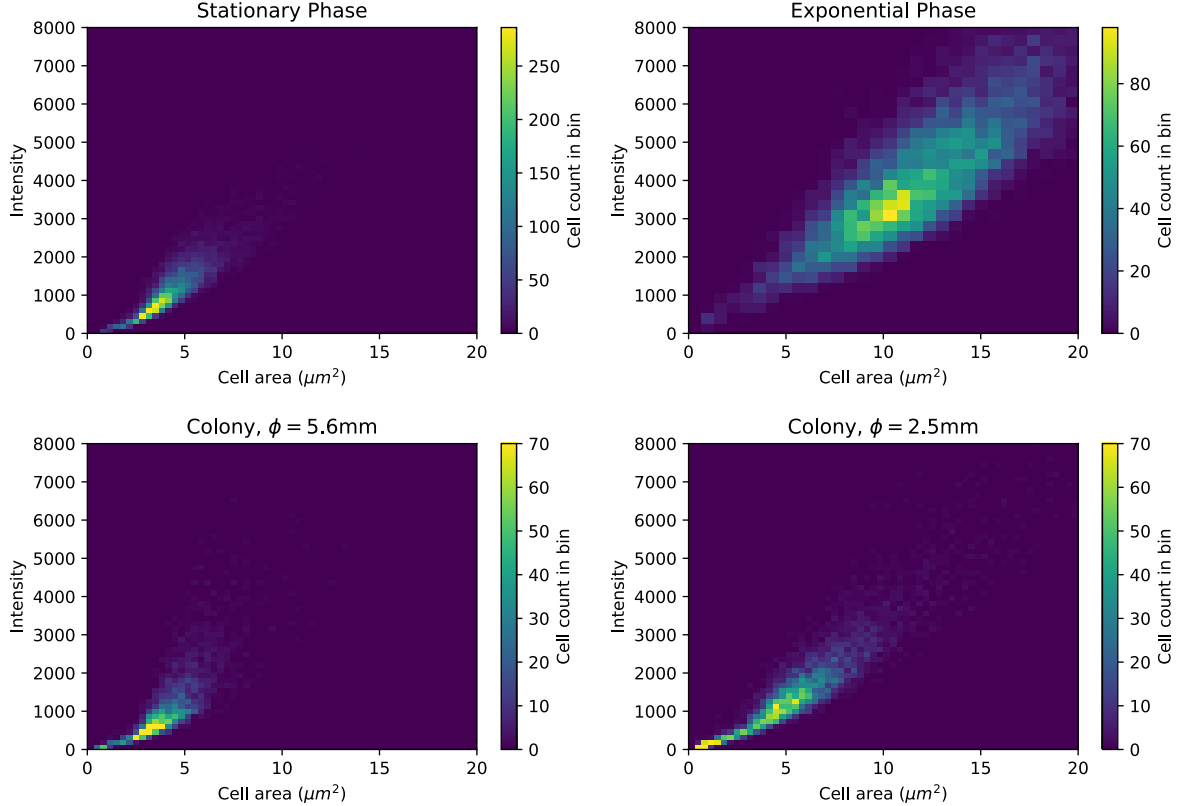


**Figure 16:** 2D histograms of cell intensities for SP, EP and two large disaggregated colonies, imaged at 40x with the DFA technique. The SP cells were obtained from an overnight culture; the EP cells were diluted 1:10,000 from the same culture 5 hours in advance of the experiment. Cells are binned in cells by both area and intensity. The EP plot uses larger bins due to its wider distribution. Intensity is the summed fluorescence pixel values over the segmented cell mask.

### 3.3 Biofilm volume from TRI vs control measurements

Figure 17 plots volume estimates from DFA counts and from layer areas (for colonies too small for DFA). Linear fits in the log-log domain are made at the immature (small) colony limit and mature (large) colony limit. For colonies whose DFA images contained fewer than  $\sim 200$  cells, these cells were manually counted. Figure 18 compares the volume estimates from DFA counts with those from TRI estimates. Again, reference volumes are estimated using layer areas rather than DFA for small colonies.

### 3.4 Results of optical simulations

A cylindrical model of a biofilm was used to obtain approximate signal attenuation profiles with distance into a scattering or absorbing medium, for both CLSM and widefield imaging modes (Fig 19).

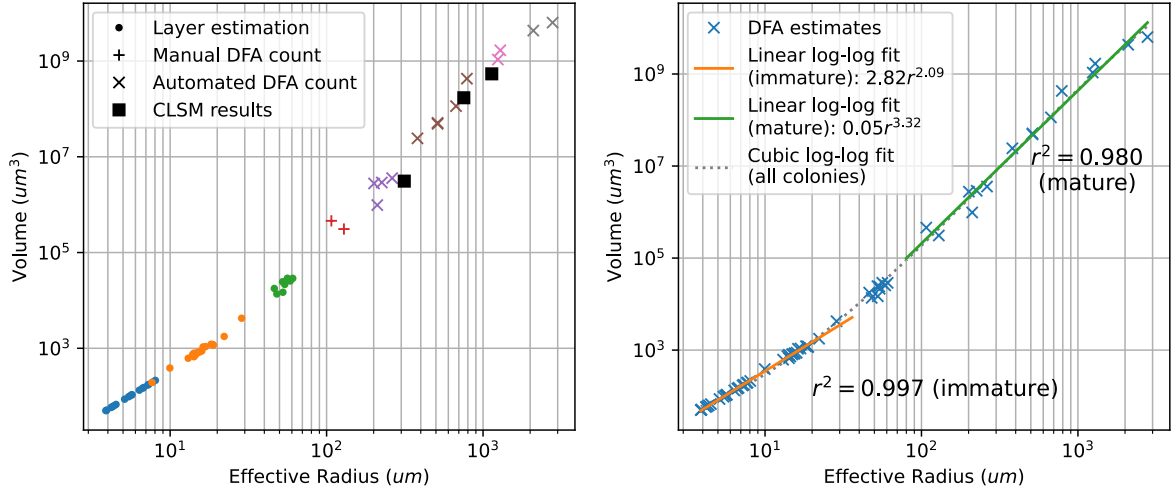


**Figure 17:** Volume of colonies vs radius based on DFA and layer-based counts. In the left-hand plot, colours refer to colonies imaged on different batches of agar plates.

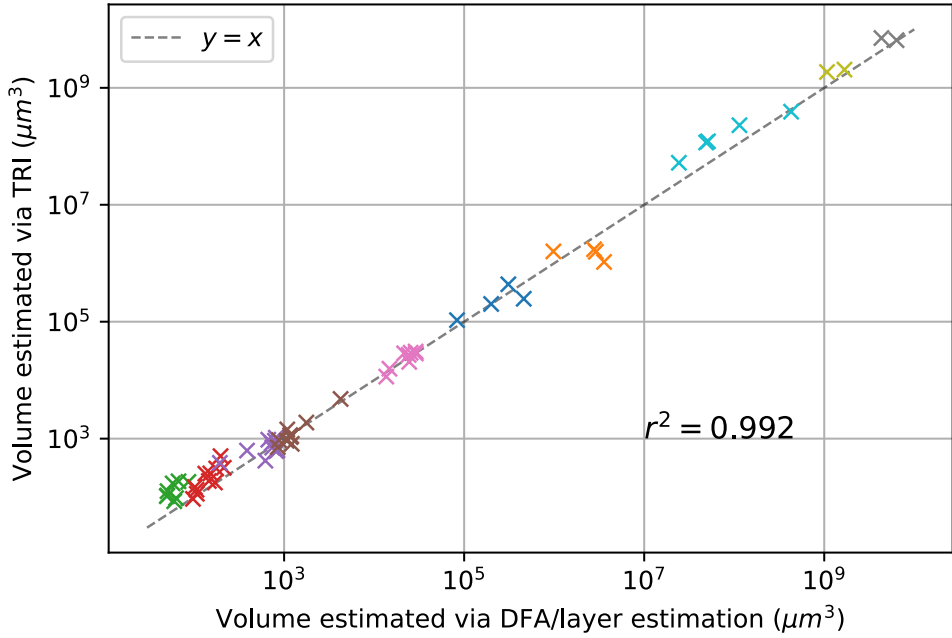


**Figure 18:** Volume of colonies obtained from the TRI vs DFA counts. The line  $y = x$  indicates perfect agreement. Colours refer to colonies imaged on different batches of agar plates.

Simulated widefield images of an entire biofilm were then captured, where the entire volume of the biofilm was uniformly excited, and the recorded volume in arbitrary units was equal to the proportion of photons detected. The normalised scattering and absorption rates were varied by increasing the biofilm's scale to show the point at which estimated volumes begin to deviate from true volumes (Fig 20).

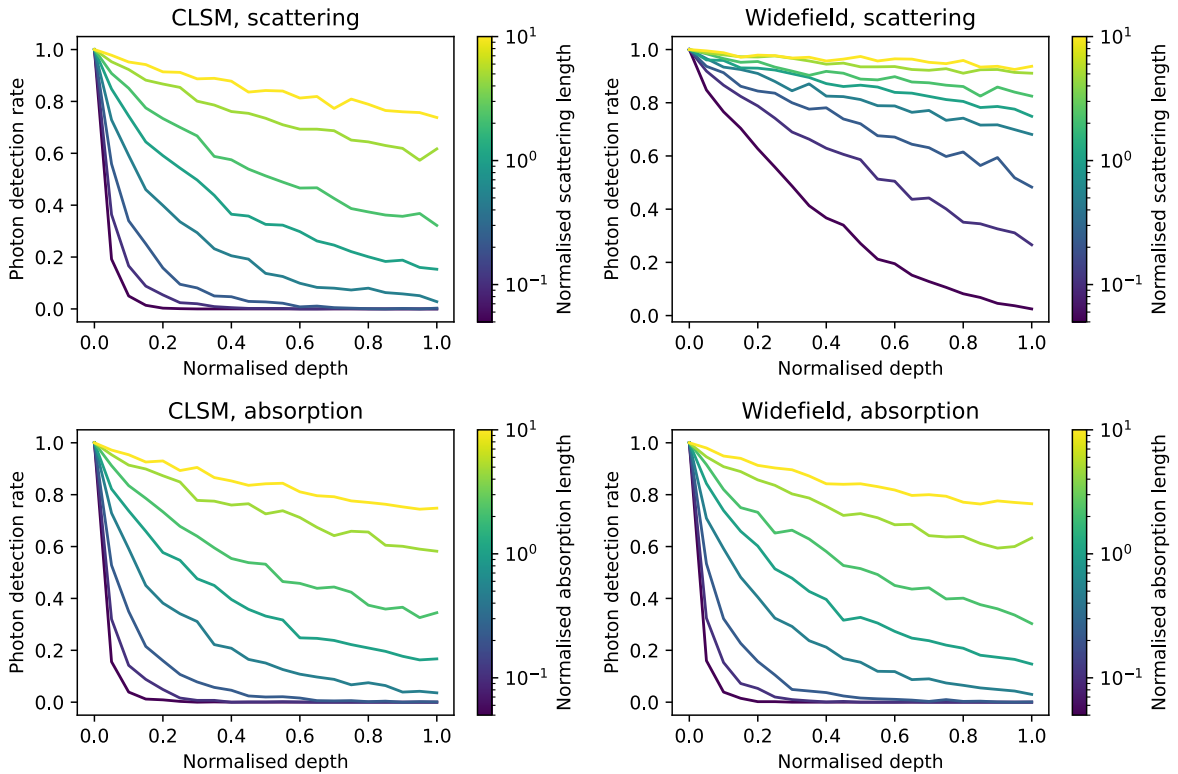


**Figure 19:** Effects of scattering and absorption as a function of depth into the sample, for both widefield and CLSM imaging. The geometry used for the scattering/absorbing media was a cylinder with very large radius and  $100\mu\text{m}$  height, with photon detection rates measured along its central axis. All variables are normalised relative to this height. The camera is focused on the z-position at which the photons are emitted.

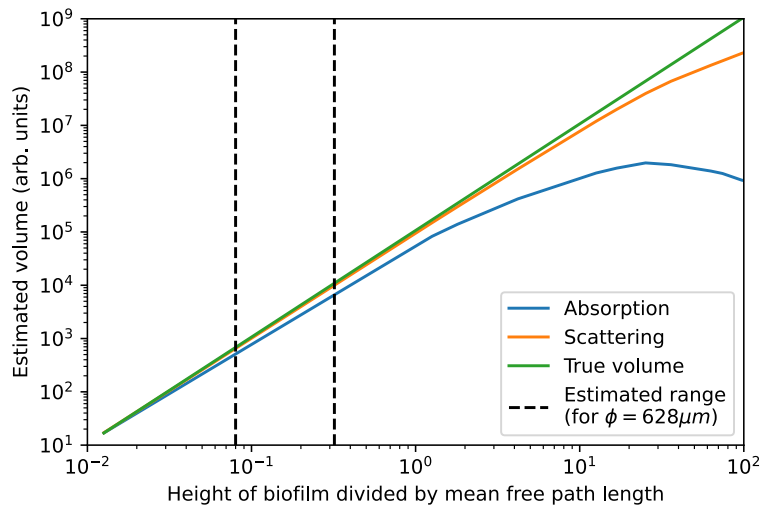


**Figure 20:** Simulations of estimated volume as function of normalised scattering and absorption lengths. The estimated range of operation for a  $627\mu\text{m}$  colony based on the CLSM scan is delineated with the dashed lines. The largest colonies studied had a height around 10x this height (based on Fig 17).

## 4 Discussion

### 4.1 Accuracy of DFA counts

Figure 15 shows that counts obtained via the disaggregation-fixation are highly linear in the log-log domain. The good fit over this large dynamic range slightly obfuscates the fact that percentage errors for individual assays have a fairly large standard deviation of 17.3%. Additionally, the best-fit exponent is not 1 (which would signify a linear proportionality between count and dilution fraction), but 0.93, meaning that a 100:1 dilution only results in a 72:1 count reduction.

Some confidence is restored by noting that a likely source of this form of bias is poor calibration of the micropipettes used in the assay. Micropipettes used for all dilution steps had not been calibrated for several years, so a constant bias to dilution ratio is unsurprising<sup>8</sup>. In addition, random error in the volume ejected may have contributed around half of the percentage error: Diameters varied with a standard deviation 4.7% (9.6% for areas), and the three counts for each dilution level were fairly self-consistent (mean standard deviation of 7.3% across samples) and were consistent with manual counts (which had mean standard deviation 8.6%). Therefore, the true accuracy of the technique can be estimated at around  $\pm 10\%$ .

Finally, despite concerns that at high cell concentrations, more error would be present due to altered hydromechanical properties or reduced segmentation accuracy, there is no clear trend to the residuals with dilution, which appear roughly Gaussian-distributed overall (Fig 15b).

### 4.2 Cell intensity and area distributions from DFA

It is immediately clear from Figure 16 that EP cells are significantly brighter and larger than SP cells, which is expected. Disaggregated cells from large colonies appear to align far more closely to SP cells than EP cells, which is also unsurprising, as the majority of cells in these biofilms are not directly in contact with the agar substrate and therefore do not receive the same nutrient flux as EP cells. It was not possible to perform the DFA technique on very small colonies, but visual inspection showed that the cells to be more similar to EP cells in morphology, due to the fact that nutrient supply is not limiting in these cases. These observations provide evidence supporting the decision to use SP cells for reference intensities with large colonies in the TRI method, but instead using the mean intensity of the bottom layer of cells for small colonies.

Despite changes to fluorescence and area distributions, it is clear that generally for SB6, as cell volume increases, total fluorescent activity received from that cell increases in a roughly linear way (using area as a proxy for volume, assuming a constant cell height). Although the smallest cell sizes violate this trend, this is also the regime where significant error is expected, due to deviations from a proportional relationship between cell area and volume as well as segmentation not exactly aligning with cell area (exacerbated by the fact that dimmer signals are harder to detect and segment accurately). It is therefore hard to draw conclusions beyond the broad trend. Additionally, there is no information about the spatial distribution of cell intensities within a biofilm: therefore, shape estimation may still be compromised, even if bulk intensity measurements are accurate.

---

<sup>8</sup>The accuracy of the 1 $\mu$ l ejection was considered extremely important for the success of the method, so a higher-accuracy micropipette was borrowed. Any bias originating from this volume ejected will have affected the coefficient of  $f$ , rather than the exponent.

### 4.3 Biofilm volume from TRI vs control measurements

Comparing volumes obtained using DFA and layer estimation with measured radii from the colony images gave a convincing growth relationship between the two variables (Fig 17), which was consistent with the CLSM biofilm data volume estimates. Percentage error from a cubic fit in the log-log domain again had a relatively high standard deviation of 26%, though this will be partly due to natural variation in colony dimensions. A linear fit to the volume-radius relationship for the small-biofilm domain yielded an  $r$  exponent of 2.09, which is consistent with colonies first expanding mostly in a single layer. A similar fit in the mature-biofilm domain gave an exponent of 3.32, implying that colonies' aspect ratios increase slightly as they get larger.

Comparing volumes obtained using TRI and DFA/layer estimation provided a compelling fit to the  $y = x$  relationship of perfect agreement, although once again, percentage error had a high standard deviation of 40%. Part of this will be due to error in the DFA measurements, while another large part is likely related to the quantification of single cell mean intensity. This measurement probably introduces a large amount of error as it is performed close to the microscope noise floor and results in a small number by which biofilm intensities are divided.

There are no signs of deviation from the linear relationship for even the largest colonies, despite the thickest colonies mean heights on the order of  $200\mu\text{m}$  (derived from volume estimates). This shows that, encouragingly, TRI does not suffer from the same penetration issues as CLSM, and that reductions in intensity due to oxygen limitation are not yet significant.

### 4.4 Results of optical simulations

Although the Monte Carlo simulations involve a simplified imaging scenario, qualitative phenomena can be explored and compared to reality in order to understand why TRI does not suffer from penetration issues. Figure 19 shows that if absorption is the culprit for diminished signal, widefield microscopy does not provide any improvement to imaging penetration over CLSM. This is because the photons do not physically leave the sample. However, if scattering is the cause, then widefield detects many more photons than CLSM, since the pinhole aperture in CLSM filters out the vast majority of scattered photons, which for widefield they are often still detected, even if they are not focused to the correct image position. The fact that there were not significant deviations for large biofilms, which would be predicted if absorption were the cause of attenuation (Fig 20), implies that scattering is likely responsible for the most part of CLSM attenuation.

## 5 Conclusions & Future Directions

The use of TRI for rapidly and non-invasively characterising large colonies has been validated as an effective in this report, and DFA has been proven as a reliable way to calculate the volume of a biofilm while also gaining information about the cells within it.

Both of these techniques, however, involve significant measurement error, on the order of 40% and 10% respectively. Time-lapse microscopy will take out some of the nominal error by fitting to a series of observed values, especially if only relative volumes or heights are required, as this takes out the dependence on the quantification of a single cell's mean intensity. Limiting focus to relative values may also be useful for one-shot shape estimation of a colony. Further optimisation of the imaging techniques used here may be able to reduce these uncertainties further.

The main disadvantage of DFA is that it does not provide information about the position of imaged cells *within* a biofilm. However, further development of the assay may allow some such information to be derived: for example, by adding bright, orthogonal fluorescent dyes or constitutively-expressed proteins to the biofilm and intentionally photo-bleaching the biofilm before disaggregation to apply a known attenuation pattern across the biofilm, the intensity of this fluorescent channel post-disaggregation could possibly be correlated with spatial position of the cell. This would be limited by the significant intrinsic expression noise and for autofluorescent cells (a ratiometric approach could deal with structured variation in expression through the biofilm).

Further investigation using the tools and data acquired during this report could investigate how the shape of the fluorescent profile compares between widefield reconstruction and the CLSM ground-truth. Two factors will primarily limit lateral resolution from this technique: scattering rate and depth of focus. This is because both scattering and out-of-focus emitters result in a blurred profile. An initial estimate from the geometry of Figure 28a is that the lateral smearing due to being out of focus is proportional to the distance from the focal plane multiplied by  $\tan \theta$ , and therefore increases with NA and the biofilm's height.

A key disadvantage of widefield fluorescent microscopy for biofilm characterisation is the large amount of data generated, especially if a large biofilm must be imaged. Image stitching and photobleaching involved in multi-point acquisition also results in complications, even with the tools developed in this report. A way to mitigate all of these effects, as well as increase lateral resolution for shape estimation, could be to use low magnification, low NA lenses for larger biofilms. Lower lens NAs (which tend to come with lower-magnification lenses) will, however, reject more light, potentially reducing depth penetration into the biofilm.

2D fluorescent microscopy clearly has distinct advantages over alternative characterisation methods for biofilms. To summarise, this is because it provides non-invasive, fast imaging that works even for large colonies. Additionally, it has the advantage of being very inexpensive, as standard lab equipment was used in protocols and many labs already possess a fluorescence microscope.

Although 2D fluorescent microscopy for biofilms is unlikely to be useful outside of laboratory situations (because of the data processing involved and the requirement of a sophisticated microscope if one is not already owned, as well as intimate knowledge of its background signal), it renders accessible - both financially and practically - much more insight into biofilm development, which will hopefully provide the key to medicines, industrial treatments and the engineering of beneficial biofilms in years to come.

## 6 Acknowledgements

I wish to thank Dr Somenath Bakshi of the Engineering Department, Cambridge University for his supervision, insightful feedback on my progress, and high-level direction of the project.

I also wish to thank the three PhD students of the Bakshi lab: Charlie Wedd, Camillo Moschner, and Georgeos Hardo, for their frequent and invaluable day-to-day help with lab training, feedback and ideas, without which this project would certainly not be what it is. In addition, I would like to thank Ali Ahmed, a fellow MEng student for laying the groundwork for this project in a summer UROP, and Temur Yunusov for dedicating time to supervising my CLSM scans.

Finally, I would like to thank Franscesca Adams for her support, for helping me to maintain some semblance of a work-life balance in this project, and for introducing me to the ImageJ Weka plugin (!).

## A Overview of biofilm characterisation techniques [40]

**Plating (CFUs).** A biofilm is disaggregated into a suspension of constituent cells. These are diluted by various factors and used to inoculate agar plates. After a period of incubation, the number of colonies is counted on a suitable plate to determine the suspension's cell count in colony forming units (CFUs) per ml. This differentiates live from dead cells, but is highly laborious and time-consuming, prone to error and bias if counting is not automated, and does not account for small aggregate or clumps of cells forming colonies.

**Counting Chamber.** A disaggregated suspension is placed in a Petroff-Hausser chamber counting slide. This can be used to determine cell counts but does not differentiate live from dead cells. The method's use with fluorescence is explored in Section 2.2.2.

**Flow-based.** A disaggregated suspension is passed through a microfluidic channel that detects their passage. Coulter counters count cells (without live/dead differentiation), while flow cytometers take laser scattering measurements of each individual cell that passes through, which are sometimes fluorescence-enabled, obtaining more information. These methods are easy and fast, though flow cytometers are expensive (\$50,000-\$100,000).

**TOC, OD & Luminometric Methods.** These methods measure the total volume in a disaggregated suspension by respectively by heated acidification/oxidation to obtain total organic carbon (TOC), use of scattering measurements (i.e. optical density, OD) alongside the Beer-Lambert law, and mixing with luciferase to generate and measure light due to ATP interactions. TOC and OD methods are only approximate and require calibration with a cell count under any new set of conditions. TOC is more accurate but instruments are more expensive (~\$20,000). For reliable results, the commercial luciferase assays should be used, costing ~\$100s per batch.

**Spectrometric Methods.** Usage of crystal violet staining or tetrazolium salts followed by disaggregation allows fluorescent spectrometry on the resulting suspension to measure biofilm accumulation. This form of technique can also be used to give bulk measurements on fluorescently-tagged molecules.

**AFM.** Atomic force microscopy (AFM) uses a micromachined tip on a cantilever, scanning the tip across a sample and measuring deflection to obtain a vertical shape profile in 2D. In tapping mode, this can be used on biofilms without disrupting growth, although there may be some surface damage. This equipment is expensive (\$10,000-\$500,000).

**QCM.** A quartz crystal microbalance (QCM) noninvasively measures the mass of biofilm growing on the device's gold or SiO<sub>2</sub> substrate from shifts to the crystal's resonant frequency.

**SEM.** Cryosectioning of a biofilm followed by scanning electron microscopy (SEM) allows extremely high-resolution imaging of biofilm interiors. However, equipment is very expensive (\$100,000-\$1,000,000), and the imaging process is destructive. Cryosectioning can also be performed with optical microscopy, enabling fluorescence measurements.

**CLSM.** Confocal laser scanning microscopy (CLSM) enables highly-resolved, non-invasive 3D acquisition of optical and fluorescence measurements. Equipment costs ~\$100,000s. Scanning at single-cell resolution is very slow and therefore only feasible for small biofilms, although at low magnification, the spatial distribution of fluorescent signatures can still be measured. CLSM is common in the literature for the study of biofilms. However, it has a limitation of depth penetration that is explored in this report.

## B Optimisation details of agar preparation

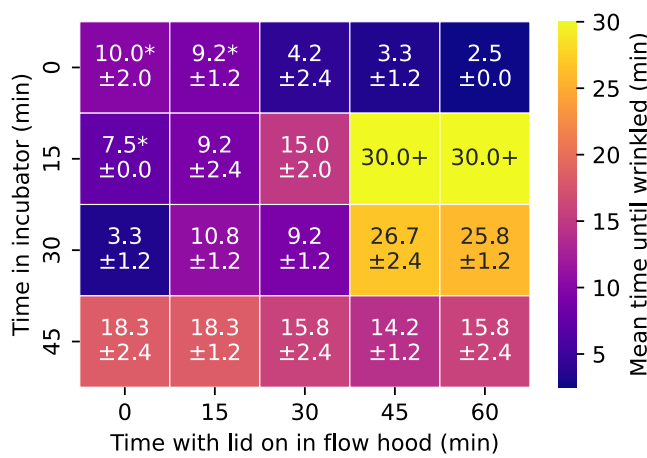
### Small-scale defects

For carrying out validation steps on individual colonies, the inter-colony spacing had to be high enough to cut out single colonies on chunks of agar. Therefore, a spatially uniform spread of  $\sim$ 10-200 colonies was required, depending on the colony size. The standard method for ensuring such a spread is to deposit a small volume of dilute culture, then either manually spread it with a plastic spreader, or gently shake with glass beads, coating them with the culture and rolling them around the plate.

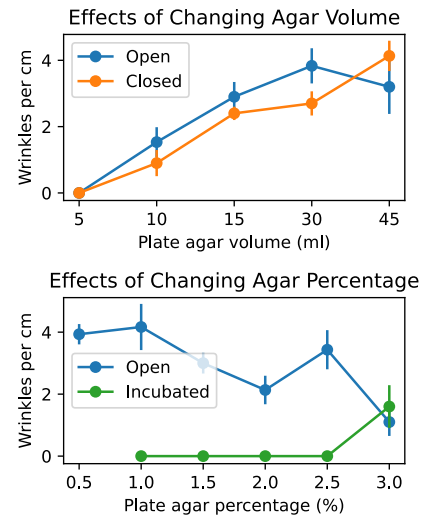
Both of these methods were found to cause surface imperfections. The former leads to microscopic line defects (Fig 5), while the latter leads to periodic dents in the surface visible to the naked eye. An alternative method was therefore devised in which a larger volume of fluid was spread across the entire plate surface, then allowed to soak into the agar substrate. After experimentation with different volumes, a technique that consistently worked was Procedure 2.

### Large-scale defects

Large-scale wrinkling can occur at the agar surface. This was hypothesised to be caused by thermal stresses induced by differential drying and/or cooling, resulting a build-up of strain energy that is released by buckling. The buckling can occur around the point of the liquid agar solidifying, or during prolonged air exposure of the surface.



(a) Time until wrinkling for different treatments. For each measurement, 3 plates were poured and checked for wrinkling every 2.5 minutes, and error values correspond to the standard deviations of their timings. Plates were not timed past 30 minutes. For values marked \*, wrinkling time was inflated because the agar was not yet solid when lid was taken off plate, so still had to solidify before wrinkling was possible.



(b) Wrinkling density vs. plate agar volume and percentage after being left open for 30 mins. “Closed” plates were first left closed for 30 mins, “Incubated” plates were first treated with Procedure 1. Vertical bars indicate range of multiple samples on the same plate.

**Figure 21:** Experiments into the effects of agar treatments on wrinkling.

Since both the inoculation and imaging methods rely on prolonged exposure of the agar to air, an experiment was conducted to determine a technique of plate preparation that would minimise wrinkling. An annealing-like treatment can be expected to reduce strain differentials. The lab did not possess an oven or incubator equipped with temperature scheduling, so the plates were left in the incubator after pouring liquid agar at 65°C for a certain amount of time, then left with the lid on in the flow hood for a further period. The effectiveness of this treatment was evaluated by measuring the time (in 2.5 minute intervals) until wrinkling was observed once the lid was taken off the plate (still in the flow hood). The two time periods were varied in a 2D grid search (Fig. 21a).

Ignoring the inflated times for treatments totalling  $\leq 15$  minutes, it was clear that increasing the total incubator and lid-on times generally increased wrinkling times. Interestingly, there was a ‘sweet spot’ of 15 minutes in the incubator followed by 30-45+ minutes with the lid on. Leaving for longer than 45 minutes did not result in improvement or deterioration to the behaviour. A possible explanation for the lack of wrinkling under this treatment is as follows: longer periods in the incubator resulted in full solidification, so that once the plate was taken out, temperature stresses built up. Meanwhile, if the plate is removed at 15 minutes, it has not fully solidified, but it *is* able to cool more uniformly. Not placing the plate in the incubator at all results in steep stress differentials during the solidification process.

Experiments varying agar volume indicated that extent of wrinkling (this time measured in wrinkles per cm) tends to increase with thickness, which is consistent with the hypothesis of stress differentials (Fig 21b). There was no clear trend of the extent of wrinkling with changing agar percentage for open plates, but using the optimised procedure all percentages in the range 1.0-2.0 showed no wrinkling - 3.0% agar may have solidified too quickly or while in the incubator (Fig 21b). 1.0% agar did not have enough structural integrity to be inoculated, and 0.5% did not solidify at all during the experiment. Using 15ml of 1.5% agar was considered a reasonable trade-off between wrinkling time, integrity and rate of dehydration, with the benefit of being fairly standard parameters. Procedure 1 then follows.

## C O<sub>2</sub> depletion calculation parameters

Parameter	Symbol	Value	Source
Yield coefficient of biomass on O <sub>2</sub>	$Y_{O_2/X}$	1.0	[41]
Diffusion coefficient of O <sub>2</sub>	$D_{O_2}$	$2.7 \times 10^{-5} \text{ cm}^2/\text{s}$	37°C, [31]
O <sub>2</sub> concentration at surface	$S_p$	6.0 g/cm <sup>3</sup>	close to saturation
Specific growth rate of cells	$X$	0.6-1.0 h <sup>-1</sup>	[42]
Cell density	$\mu$	0.021 g/cm <sup>3</sup>	[41]

## D Optimisation details of DFA

### D.1 Fixation technique

The following methods were tested for fixing cells.

- **‘Agar Sandwich’ method.** This involves dropping 800μl of agar onto a 22×22mm cover slip, placing another slip on top when it has solidified just enough to adhere and create a flat surface, then waiting for this to fully solidify, taking the top slip

off, dropping some volume of cell suspension on the agar, waiting for it to adsorb and flipping the ‘sandwich’ over onto a microscope slide. This has the advantage of immobilising cells in a highly flat field of view. However, the ‘sandwiches’ are difficult and tedious to create, and dry very quickly due to the small amount of agar.

- **Immobilise on agar plate.** Dropping a small volume directly onto a plate and waiting for it to adsorb addresses the drying issue and is much easier to prepare, as a plate is easy to pour out and can be used many times. However, imaging through the agar and plastic plate compromises image quality.
- **Flipped agar chunk.** This method once again uses an agar plate; however, after cells have adsorbed onto the agar, a chunk is cut out with a sterile knife and flipped onto a cover slide. This combines the strengths of the previous two methods.

The final method was picked, as it provides a good compromise of throughput and ease. M9 agar was used, both to avoid further growth of cells and to minimise autofluorescence of the agar. Pouring the plate via the Protocol 2 ensures flatness.

## D.2 Method of disaggregation

Typical techniques in the literature for biofilm disaggregation use some combination of scraping, vortexing, homogenisation, and sonication. The precise disaggregation method has a large effect on numerical outcomes, and has been historically optimised only in particular applications (e.g. [43], [44]), but has been subject to some recent attention in the general case [45].

In this case, disaggregation is particularly straightforward, because SB6 does not produce EPS to the extent of other organisms, so cells are not tightly bound either to the surface or each other. However, the typical substrate for biofilm enumeration is a hard surface. The fact that agar was used in this study presented an issue in that the agar itself can break up under treatment, interfering with the imaging process<sup>9</sup>.

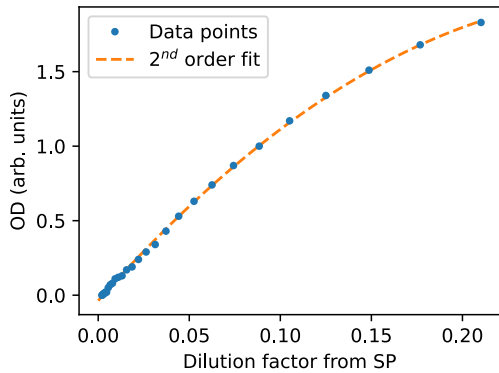
Therefore, the effects of different agar treatments were investigated on the extent of colony removal and damage to the agar. For these tests, disaggregation was performed within a cuvette. This was done because alternatives such as eppendorf tubes caused agar damage due to their curved edges, because imaging could be performed on the agar slab directly through the cuvette’s flat sides after treatment, and because optical density measurements were made trivial to perform, allowing approximate comparisons of extent of disaggregation. An approximate optical density calibration curve was obtained by performing a serial dilution of SP cells into M9 media, so that ratios of cell counts could be roughly estimated using OD data (Figs 22a,b).

The main treatments applicable to these samples were washing, vortexing and sonication. Various combinations of sonication followed by vortexing were tested, with each case preceded by washing the samples in the M9 media that they were treated in<sup>10</sup>. Colonies

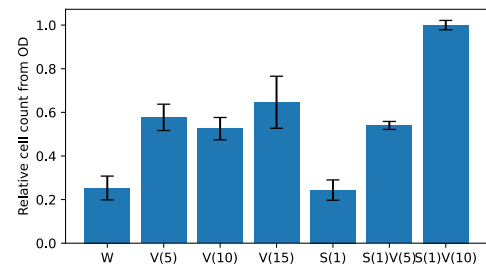
---

<sup>9</sup>There were two main problems. The first was that small chunks of LB agar make segmentation more difficult because of LB’s autofluorescence. The second was that, during imaging, cells can sit on top of large chunks of agar, bringing them out of focus, complicating both enumeration and intensity/shape calculation.

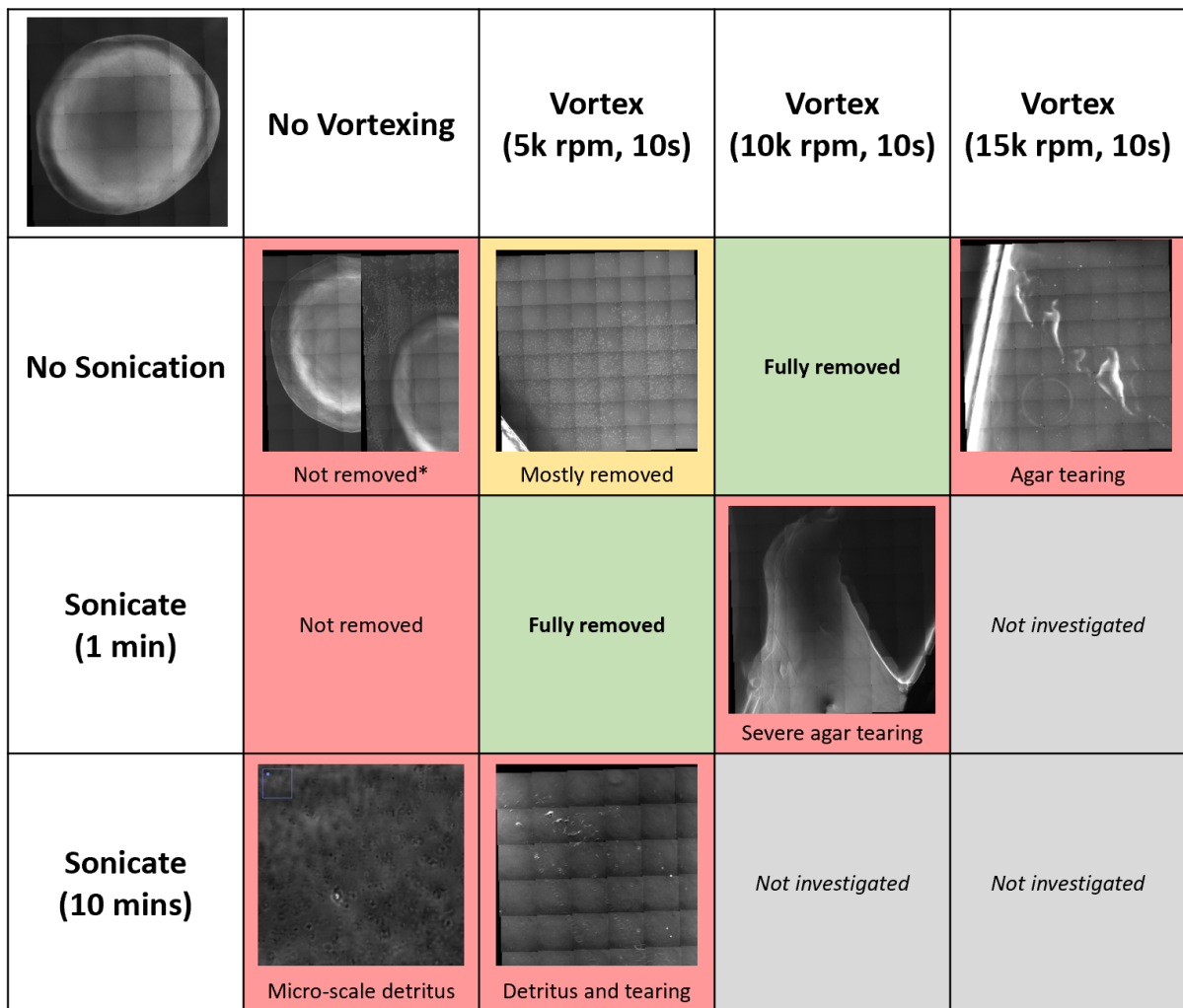
<sup>10</sup>Centrifugation was also investigated but caused significant damage to the agar and did not guarantee that all cells were gathered in the pellet.



(a) OD calibration curve with second order polynomial fit, via serial dilution from SP.



(b) Histogram of approximate relative cells/ $\mu\text{m}^2$  of colony via OD measurements. W: washed only, V( $x$ ): Vortexed for at  $x$ k rpm, S( $x$ ): Sonicated  $x$  minutes.



(c) Matrix of different treatments tested for disaggregation. In each case, washing was applied first, followed by sonication, followed by vortexing. 3 colonies were subjected to each treatment. Top-left cell indicates a typical colony pre-treatment. Images are representative Phase Contrast microscope grid acquisitions, with  $374.4\mu\text{m}$  square FOVs that are have been stitched together without image correction applied. For cell marked \*, colonies were only washed. Interestingly, it was found that an outer layer of cells was washed away, leaving a ‘core’ attached to the agar substrate (left side is before treatment, right is after).

Figure 22: Biofilm disaggregation treatment analysis.

used for tests were approximately 1000 $\mu$ m in radius, and they were washed in 750 $\mu$ l of M9 media.

It was found that washing or sonicating alone were insufficient for removing colonies from the agar, that vortexing at >10,000 rpm caused damage to agar, and that this threshold was reduced while also creating micro-scale detritus that inflated the OD measurements when vortexing was performed after sonication (Fig 22b,c). Appropriate treatments included vortexing at 10krpm for 10 seconds or sonicating for one minute then vortexing at 5krpm for 10 seconds (detritus was not visible in this case). Although the sonication step potentially has the added benefits of breaking up small cell aggregates in the resulting suspension, it was avoided in case of unseen detritus.

### Protocol modifications

For small colonies, disaggregation is easier, but the total cell count is lower, which is likely to introduce significant error into this technique when suspensions are very dilute. Therefore, smaller volumes of M9 media were used for washing and vortexing (down to 200ul).

For large colonies, disaggregation is more difficult. It was found that continued vortexing would eventually disaggregate colonies up to the largest size tested (up to 5mm diameter). Therefore, the vortexing time was extended to up to a minute in these cases. Agar chunks were tested to verify that this did not cause agar damage.

### Notes on preparation of M9 agar

M9 media is a form of minimal salt media that cells cannot grow in without a source of carbon, but that does not cause osmotic lysis [46]. It is a thermostable medium, so can be sterilised by autoclaving. However, although it is not thermosensitive on its own, it was found that when mixed with agar and autoclaved, a reaction occurred that resulted in the solution (and resulting solid agar) turning an opaque grey. This reaction also progressed gradually if the two substances were held in a 65 oven for prolonged periods (~12+ hours). A simple method for pouring a transparent plate of M9 agar on demand was found to be:

### Procedure D1: M9 agar preparation

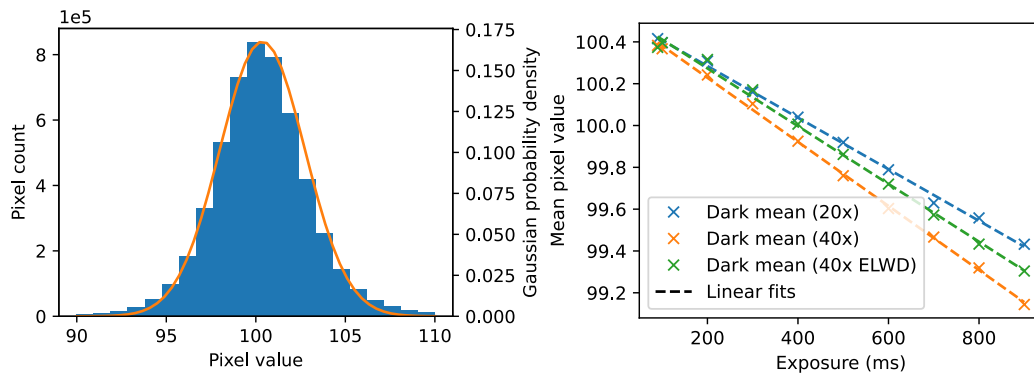
1. Prepare half-volumes of agar solution and M9 media separately, both at double concentrations.
2. Autoclave both solutions, and store for as long as required.
3. When a plate is needed, heat the agar to melting, ensuring that the concentration is uniform and that all the agar has melted by heating and shaking repeatedly.
4. Mix together the two solutions at a 1:1 ratio to the desired volume, and pour immediately.

## E Details on microscope image intensity correction

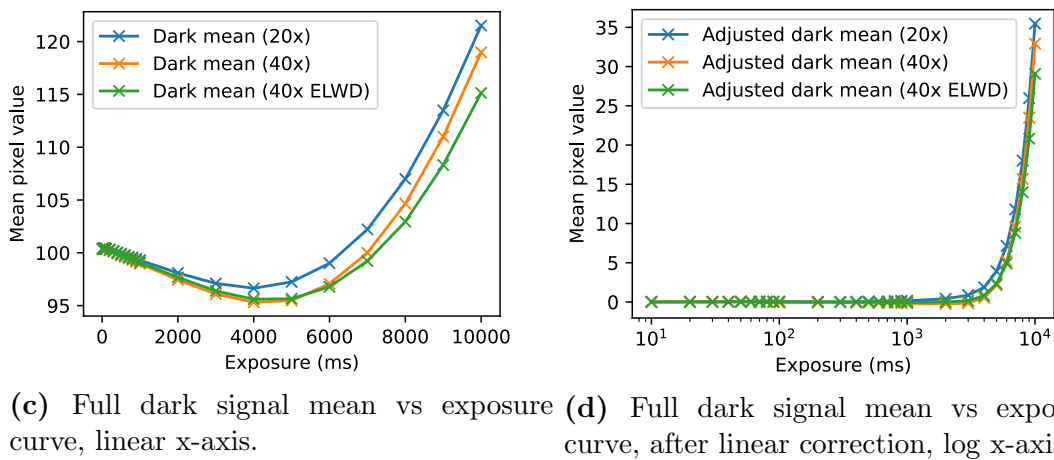
### E.1 Dark signal

At the limit of low exposures, the signal approaches an image of purely Gaussian noise with a mean of 100.4 (in arbitrary intensity units) and a standard deviation of 3.2 independent of the lens used (Fig 23a)<sup>11</sup>. In symbolic terms, the ‘mean-image’ was  $100.4I_0$  where  $I_0$  is an image of ones. This is a combination of thermal and read noise [35], that has likely been calibrated with an voltage bias to provide a mean of around 100. This limiting value (i.e. 100.4) was confirmed for imaging situations with zero beam power, 100% beam power but a black matte material on the scope, and 100% beam power with LB agar, by observing the trend with reducing exposure.

Correlations in pixel intensities do exist in the form of horizontal ‘streaks’ due to the way in which pixels are read. This is unavoidable and not a significant problem. However, it was ensured that the CCD acquisition mode was always set to ‘Ultra-low noise’ to avoid horizontal step artefacts in the mean background value that would arise with faster acquisition modes.



(a) Distribution of dark signal pixel values (at 100 $\mu$ s exposure). (b) Linear part of dark signal mean vs exposure curve.



(c) Full dark signal mean vs exposure curve, linear x-axis. (d) Full dark signal mean vs exposure curve, after linear correction, log x-axis.

**Figure 23:** Analysis of dark signal.

<sup>11</sup>The pixel values fail D’Agostino and Pearson’s normality test with a statistic of 0.0, but this is due to discretisation.

A plot of image mean against exposure at zero beam power (Fig 23b,c) shows an initial linear *decrease*, which at first seems surprising. It is a consequence of a constant level of pixel read noise being diluted over the increased exposure time, and can be expected to remain linear with exposure [35]. Therefore a straight line was fit to the decrease and all pixels corrected by the constant offset and linear fit (Fig 23b). As exposure increases further, however, the mean value rockets upwards. This is due to a form of ‘pattern noise’, i.e. noise that varies spatially and has a nonzero temporal mean, called dark current non-uniformity (DCNU). DCNU is due to particular pixels not responding identically to stray electrons [47], and manifests as a fixed intensity pattern that rises rapidly at high exposure in a nonlinear way. Plotting a set of exposures shows that in the case of the CCD in this microscope, DCNU results in a bright ‘frame’ image  $I_d$  at the top and bottom of the image that is independent of beam power (see “Exposure Adjustment” in Fig 9).

DCNU was corrected for by obtaining a sequence of 10s exposures, correcting for the linear trend and constant offset, taking the median across the image stack (but without averaging spatially over images, to preserve individual pixel responses), then finding the scale factor by which the resulting image must be subtracted from other linearly-corrected images captured with zero beam power and varying exposure, to minimise the variance in the resulting pixel values. This was done for exposures of 1ms, 2ms, 3ms, ..., 10ms, 20ms, etc., up to 10s. A linear interpolation was used as a ‘lookup function’  $f_d(t)$  for the scale factor to correct dark signal with unseen exposures.

Figure 24 shows that this adjustment results in less variation in the mean pixel value with exposure, reduced standard deviation and reduced skew. The nonzero skew for intermediate exposures implies that DCNU may kick in at different points for different pixels, so that full correction requires a stack of images to be taken at every possible exposure. This was not done due to project time constraints.

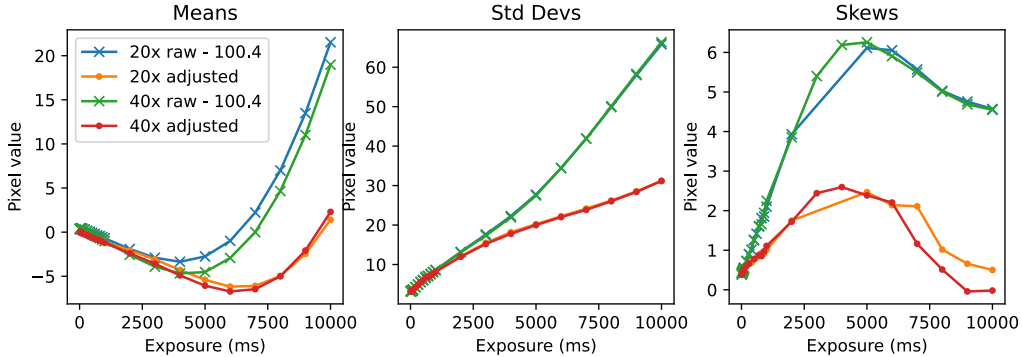


**Figure 24:** Distribution statistics of the images produced by DCNU correction (without incorporating linear correction).

## E.2 Beam leakage

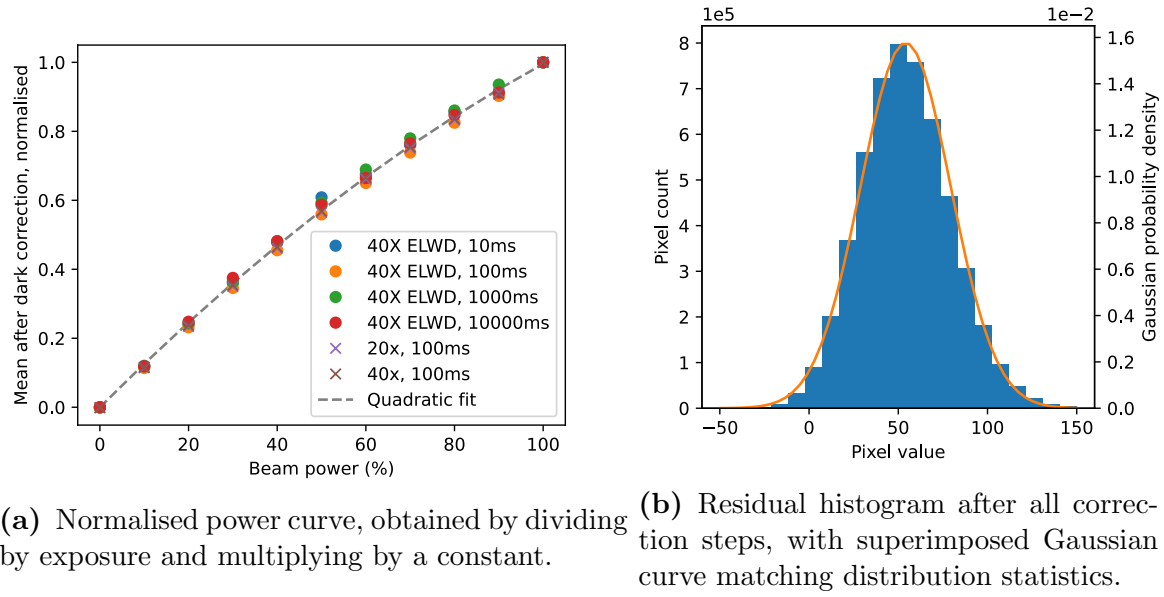
Increasing the beam intensity from zero to full (100%) with either a matte object on the imaging platform or no object at all resulted in an increase in pixel intensities. This was assumed to be due to some of the excitation beam erroneously being transmitted through or around the dichroic filter - another form of pattern noise (see Fig 9 for the beam leakage profile). Since this should be independent from any intensity received at the emission wavelength, it can be directly subtracted from pixel values.

It was found that this signal is linear in exposure and independent of the objective lens used: Dividing by exposure and normalising by a constant scale factor to the range 0-1 causes signal means to collapse to one curve (after dark correction). A power curve,  $f_p$ , was obtained with a quadratic fit through all of these data points, forced to pass through the origin. Correction for this effect was performed by multiplying a beam leakage image  $I_l$  by the exposure  $t$  and the corrected power  $f_p(p)$ , and subtracting the result.

### E.3 Beam profile

Assuming no other significant sources of pattern noise, the remaining pixel values reflect a zero-mean “shot” noise on top of signal derived from light at the emission wavelength. There remains one more form of nonuniformity in the image, however. Emission intensities are (ideally) proportional to the incident excitation intensity, which is itself nonuniform due to the large FOV and finite beam width<sup>12</sup>.

This can be corrected for by dividing by the excitation beam profile, resulting in normalised fluorescence readings  $S' \propto S$ . Additionally, assuming that signals are again linear in exposure and corrected beam power  $f_p(p)$ , dividing by these values should produce a universal normalised intensity, transferable between imaging parameters.



(a) Normalised power curve, obtained by dividing by exposure and multiplying by a constant.  
(b) Residual histogram after all correction steps, with superimposed Gaussian curve matching distribution statistics.

**Figure 25:** Further results of image correction investigations.

Unfortunately, obtaining this beam profile is not trivial. It may be slightly warped by the precise imaging setup (i.e. depending on distortion agar thickness and composition)<sup>13</sup>. Additionally, there is a fluorescent signal background due to agar autofluorescence.

Conveniently, these problems somewhat solve each other: for every agar plate that was imaged, a set of 16 empty agar ‘background’ images was captured. Assuming agar

<sup>12</sup>One final other contaminant that may be present is pixel response non-uniformity (PRNU). However, this will manifest in exactly the same way as beam profile non-uniformity, so is absorbed into beam profile correction.

<sup>13</sup>It was also different for different lenses. For the 20x lens, it resulted in a radial profile. Unexpectedly, for 40x and 40x ELWD, there was instead a profile that increased roughly linearly with distance down the image. This may have been due to problems with lens alignment/calibration.

generally has a uniform fluorescence  $\alpha$ , taking the median of this image stack should give a good measurement proportional to the beam profile. As a final correction step, each image was divided by this profile. In the case of DFA images, a median was simply taken across the full set of images over the droplet footprint. Since cells are sparse compared to the background, the median operation rejects their high (outlier) intensity values and recovers a background profile.

This finally yields an image that is at least proportional to the desired fluorescent signal  $S(x, y)$ . Derived values in different imaging runs should be comparable if the agar autofluorescence background  $\alpha I_0$  is equal between them. Residual noise from the correction of an agar-only image appear consistent with a Gaussian distribution (Fig 25b), implying that the correction procedure carried out has dealt with most other obfuscation of the signal. However, it should be noted that in some ‘corrected’ images there were small gradients and deviations from a uniform-mean background (up to  $\sim 10\%$  of the image mean).

## E.4 Image stitching correction

Large regions could not be captured at an appropriate resolution in a single field of view, so much of the acquired data was obtained by scheduling a grid of locations at which to capture images. Although the microscope was capable of moving consistent and specified distances, the real-world distances moved were not exactly those requested, and the movement drifted at a constant angle of  $2^\circ$ . This is almost certainly due to miscalibration of the microscope with respect to the stage. The parameters required to convert these to true distances were calculated by taking a set of images with different overlaps and using an established image stitching algorithm, MIST, to align them [48]. Successive images were stitched using these parameters.

## E.5 Photobleaching considerations

Investigations into photobleaching showed that:

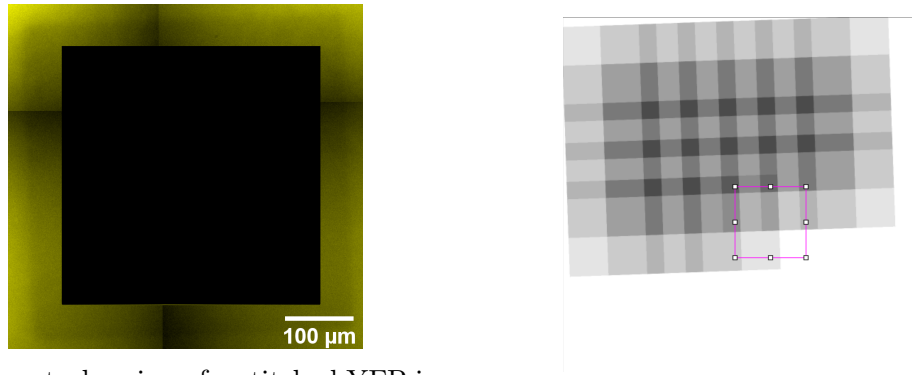
- The excitation beam directly illuminates a square region of the sample, concentric with the FOV, but with a side length 22% greater (and angled at  $2^\circ$  due to the stage miscalibration). Therefore, if the entire colony is imaged, surrounding FOVs are always photobleached to some extent in a ‘halo’ around the imaged portion (Fig 26a).
- In addition to direct illumination, there is a lessened but noticeable long-range photobleaching effect under consistent illumination that gradually decreases the mean image intensity, likely due to internal scattering and reflections. This effect can be significantly reduced by ensuring the excitation beam remains off during microscope travel between image captures.

Not realising the extent of the excitation ‘halo’, acquisition for large colonies was set to have a movement distance of  $200\mu\text{m}$  (46.5% overlap), assuming that this would mean that any part of the biofilm would be bleached only by neighbouring FOVs. Instead, there were longer-distance interactions between FOVs due to this extended region of photobleachings, severely complicating correction algorithms.

Therefore, more crude and heuristic methods were used for obtaining the TRI of large, stitched colonies. Approximating the photobleaching profile as constant over the known

'halo' geometry, the imaging process was simulated over a region of constant intensity (Fig 26b). The photobleaching ratio of a single capture (approximated as a multiplicative attenuation constant) was estimated by taking FOVs from the central part of a large colony, and dividing the mean intensities of 100x100px regions subject to zero and one rounds of photobleaching according to this simulation, respectively. This ratio, 0.922, was then used for the simulation and the average attenuation of a typical FOV (i.e. in the interior of the biofilm) was calculated, obtaining a value of 0.832. Net TRI values for large colonies were then divided by this value (all such colonies used the same exposure and beam power).

Of course, the easiest method of dealing with photobleaching is reducing beam intensity and exposure as much as possible: the images captured of large colonies used a low exposure, but these parameters could have been reduced further while maintaining a good signal-to-noise ratio in future experiments. This would also reduce photobleaching during the course of a single exposure.



- (a) A central region of a stitched YFP image of a colony (without image correction). The area of the black square was previously imaged for 10s at 100% beam intensity. An angled, dimmer 'halo' can be seen around the square caused by photobleaching.
- (b) Estimation of the net photobleaching on an average FOV. This differs for FOVs on the top, left and right edges, but the vast majority have the same net amount of photobleaching.

**Figure 26:** Illustration of photobleaching profile.

## E.6 Image correction code

Python code was written for an `ImageCorrector` object with a `ImageCorrector.imread()` method that can be used to obtain a corrected image directly from a file path, using image metadata to obtain exposure, lens and beam power information as part of the correction process.

A separate `ImageGraph` object was created for stitching an image grid. On construction, it takes an image stack or filepath (if a stack is passed, file metadata must be passed separately). The relative positions of these images are automatically calculated using the commanded grid step size, and capture locations are represented as nodes in a `NetworkX` graph object, with edges representing image overlaps [49]. This allows for convenient manipulation of the images, including stitching at full scale or with resized images (for computational efficiency), multiple types of blending at overlaps, and the ability to solve systems of linear equations allowing for small corrections to individual images to minimise the overall sum of squared errors between overlapping pixels.

The latter feature was implemented to aid with photobleaching correction. This is because it was initially assumed that photobleaching would only occur within, or very near to, previously-imaged FOVs, and the capability would therefore aid with estimating the attenuation factor/profile due to bleaching. Unfortunately, this capability did not see much use in practice, due to the longer-than-expected range of photobleaching.

## F Overview of fluorescence microscopy optics

### F.1 Widefield microscopy [50]

In widefield fluorescence microscopy, a sample is illuminated at the excitation frequency for fluorophores of interest. Once excited, these fluorophores emit photons approximately isotropically at a longer, lower-energy emission wavelength [51]. This light is gathered and focused by the microscope objective lens. A dichroic mirror within the microscope acts as a filter, reflecting light at the excitation frequency to direct it towards the sample, but allowing incoming emission light to pass through and reach a CCD camera array.

The lateral resolution  $\Delta x$  is normally limited by diffraction phenomena, as is the depth of focus (DOF),  $\Delta z$  - a measure of the axial band width about the focal plane in which the sample is sharply resolved. Both of these parameters can be expressed in terms of the Numerical Aperture (NA) of the objective lens, the wavelength of light emitted<sup>14</sup>  $\lambda$  and the refractive index of the material between the microscope objective and the sample  $n$  (typically air for non-invasive biofilm imaging, so  $n = 1$ ) [52]:

$$\Delta x = \frac{1.22\lambda}{2NA} \quad \Delta z = \lambda \frac{\sqrt{n^2 - NA^2}}{NA^2} \quad (1)$$

The NA of the objective is equal to the sine of the half-angle  $\theta$  formed by a cone of light at the focal plane (see Fig 27), multiplied by  $n$ . It can be increased to a maximum of 1 ( $\theta = 90^\circ$ ) in air, to maximise lateral resolution of the microscope, with fluids such as oil that have high  $n$  used to increase beyond this barrier. Higher-magnification microscopes require a greater NA. Unfortunately, increasing resolution results in a corresponding decrease to DOF, down to a few hundreds of nanometres for 40x lenses (Table 1). This does not mean only a thin layer within biofilm will only be imaged: Signal from out-of-plane is smeared out, but still superposes when there is for instance a uniformly fluorescing layer, rather than a point source. This is *not* the case, however, for CLSM.

### F.2 Confocal Laser Scanning Microscopy [53]

In CLSM, a very small pinhole aperture is used to block the majority of out-of-focus light. In addition, a laser excites only a small region of 3D space. This laser is scanned across a “z-stack” of x-y planes throughout a region of interest, and a highly sensitive detector receives the photons that pass through the aperture, building up a volume image.

The higher proportion of rejected light makes CLSM significantly less sensitive, requiring higher excitation powers and therefore resulting in more cytotoxicity and photobleaching than conventional 2D microscopy. In addition, the fact that x-y planes are scanned instead of captured in parallel drastically increases acquisition time, which becomes proportional to the volume being captured (rather than being constant for a given exposure).

---

<sup>14</sup>This is  $\approx 530\text{nm}$  for the fluorescent protein used here (Fig 3).

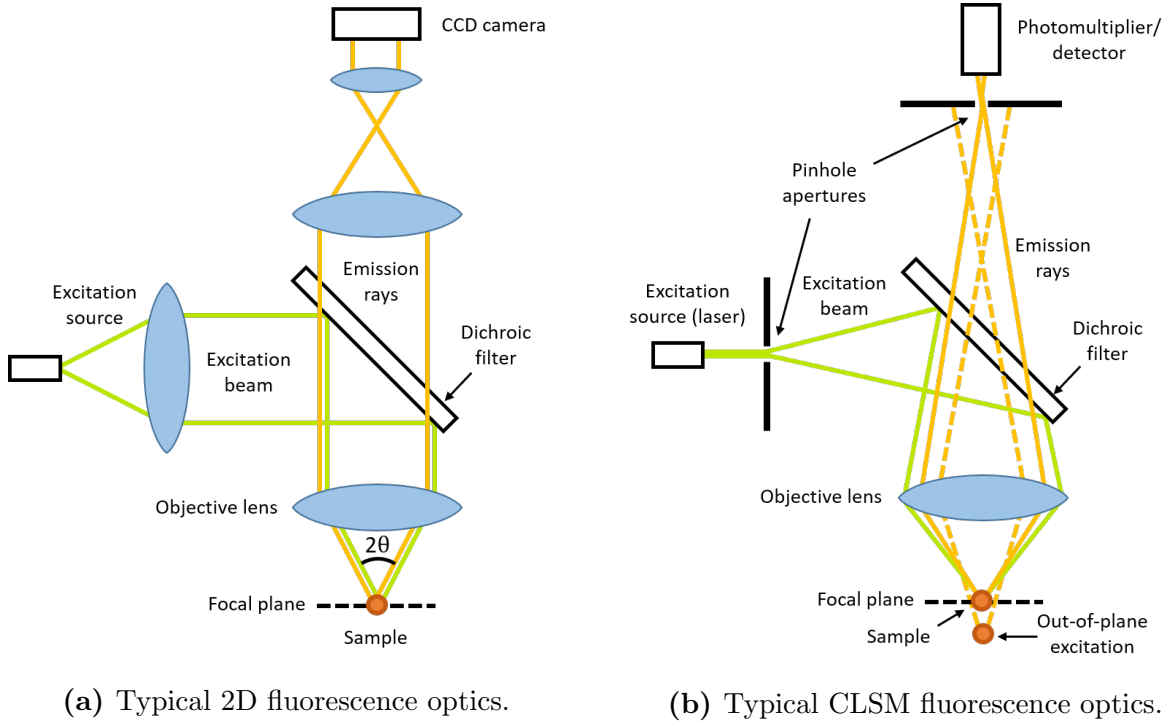


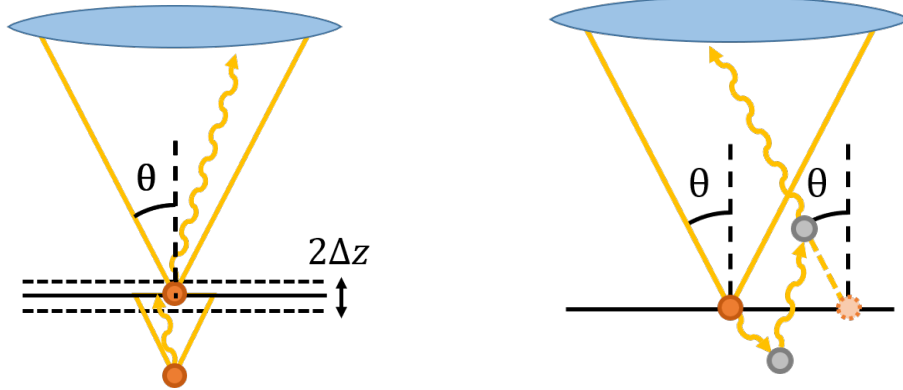
**Figure 27:** Optics comparison between 2D fluorescence microscopy and CLSM. The combination of laser illumination and pinhole aperture in CLSM result in much greater rejection of out-of-plane signals. Note that many scientific 2D microscopes, including the one used in this study, utilise Kohler illumination instead of the excitation optics shown in (a). In brief, this results in collimated (parallel) rays exciting the sample, giving a more even illumination, while the path of emitted rays is left unaffected.

time-lapse scanning at single-cell resolution for anything but very small ( $\approx 50\mu\text{m}$  diameter) samples is therefore infeasible, due to development of the biofilm during acquisition.

### F.3 Other optical effects

Distortion of point sources can be caused not only by out-of-focus emitters, but also by optical interactions within a biofilm, which is far from an idealised homogeneous medium. While the effects of axial blurring are readily modelled by an optical point-spread function (PSF), which approximates the imaging process as a linear 3D-to-2D convolution operation, other optical interactions are inherently non-linear if significant.

Scattering, in particular, can be expected to play a dominant role within a biofilm, due to the wavelengths of light used for fluorescence measurements being on the order of a bacterial cell's width. Scattering will also result in a blurring effect, but the extent of blurring is dependent on the geometry of the biofilm and the emitter's location within it. Other optical effects that may be significant are refraction at cell walls, and absorption of emitted light. Much like with out-of-plane sources, CLSM can be expected to reject the vast majority of light that does not travel in a direct line from the point source. This results in an attenuation with depth into the biofilm. Widefield fluorescence, on the other hand, may be somewhat robust to these effects. This will be explored in Section G.



(a) Diagram of the blurring of emitted photons into the focal plane from an out-of-focus point source.

(b) Diagram of the blurring caused by scattered photons.

**Figure 28:** Simplified diagrams of the blurring effects of axial position and scattering.

## G Optical Monte Carlo simulation procedure [39]

In an isotropic medium with scattering rate per unit distance  $\mu_s$  and absorption rate  $\mu_a$ , the overall interaction rate is  $\mu = \mu_s + \mu_a$  and the travel distance  $x$  between interactions follows an exponential distribution  $\mu e^{\mu x}$ . When an interaction occurs, the probability that the event is scattering rather than absorption is  $p_s = \frac{\mu_s}{\mu_s + \mu_a}$ , with  $p_a = 1 - p_s$ . Between scattering events, path lengths are drawn from the exponential distribution via a transformation function  $-\frac{1}{\mu} \ln v$  on a uniform random variable  $v \in [0, 1]$ . The event is considered scattering if another uniform random variable  $u < p_s$  (where again  $u \in [0, 1]$ ), else absorption. These rates are more intuitively parameterised in this context by their inverses  $l_s$ ,  $l_a$ , which correspond to mean free path lengths between scattering and absorption events respectively.

The scattering distribution used here was the Henyey-Greenstein phase function [54]:

$$\theta = \cos^{-1} \left( \frac{1 + g^2}{2g} - \frac{(1 - g^2)^2}{2g(1 - g + 2gv)^2} \right) \in [0, \pi] \quad (2)$$

where  $g$  is the scattering angle's mean cosine (set to 0.85), and  $v$  is drawn from a standard uniform distribution,  $v \in [0, 1]$ . The directions were represented with unit vectors initialised randomly by drawing and renormalising from an isotropic 3D Gaussian, and the new direction was determined given  $\theta$  by drawing a new random vector, taking a cross product to obtain a random perpendicular rotation axis, then rotating by  $\theta$  anticlockwise about this axis.

If the photon exits the biofilm, it is treated as a ray from there onwards, with unit orientation vector  $n_x$ ,  $n_y$ ,  $n_z$ . If it has a component in the direction of the detector, the emission direction is tested for whether it is within the detector's collection solid angle:

$$\sin \phi = \sqrt{n_x^2 + n_y^2} \leq \text{NA} \quad (\text{for acceptance}) \quad (3)$$

For the purposes of this simulation, refraction on exit of the biofilm was neglected (i.e.  $n_1 = n_2 = 1$ ), as the increased model complexity was not feasible given project time constraints. If collected, an image position  $x_d$ ,  $y_d$  of the ray is calculated. For a

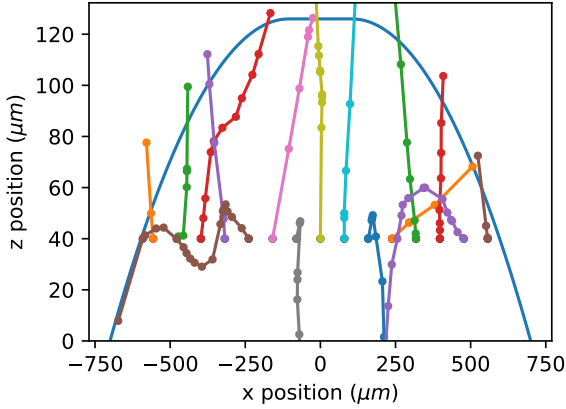


**Figure 29:** View in  $x - z$  of simulated 3D photon trajectories originating from a 1d line profile oriented in the  $x$ -direction within a biofilm.

photon emitted at angles  $\alpha_x$  and  $\alpha_y$  projected onto the  $x$ - $z$  and  $y$ - $z$  planes respectively, at a horizontal interface from refractive index  $n_1$  to  $n_2$ , this is found by

$$x_d = -x - \sin(\alpha_x) \left( z + \frac{n_1}{n_2}(d - f) \right) \quad (4)$$

$$y_d = -y - \sin(\alpha_y) \left( z + \frac{n_1}{n_2}(d - f) \right) \quad (5)$$

where  $x, y, z$  is the current position of the photon,  $d$  is the distance of the interface from the lens, and  $f$  is the focal length of the lens. The refractive index within a biofilm has unsurprisingly been found to be close to water,  $n_1 \approx 1.33$ .  $\sin \alpha_x$  and  $\sin \alpha_y$  are calculated as  $n_x / \sqrt{n_x^2 + n_z^2}$  and  $n_y / \sqrt{n_y^2 + n_z^2}$  respectively.

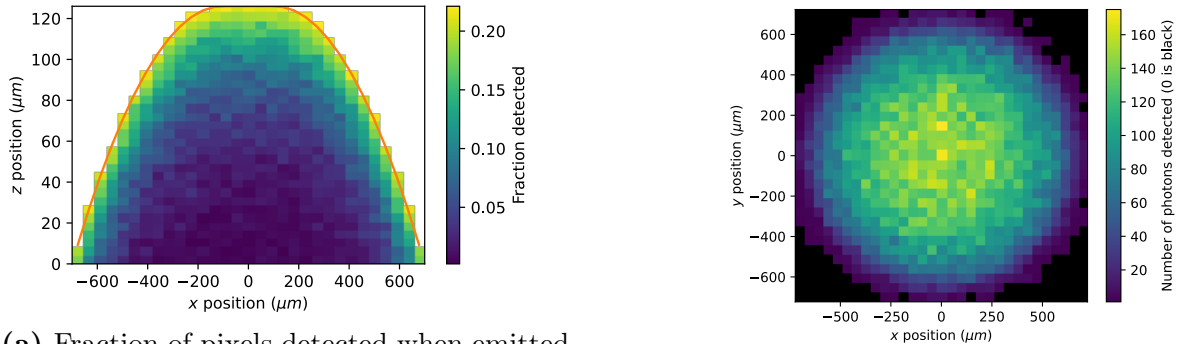
For both CLSM and widefield simulations, excitation nonuniformities due to scattering were neglected for simplicity. In the CLSM case, laser excitation is expected to have very good penetration in comparison to the emitted light, and in the widefield case the wide-beam, uniform illumination is expected to remain broadly uniform in the presence of scattering. For absorption, an approximation was taken that light will have to travel approximately the modelled path length in the medium, so the number of collected photons was reduced by an additional factor.

For computational efficiency, photons were only emitted if their  $z$ -component was in the direction of the detector. Similarly, photons scattering more than  $50 \times \Delta z / l_{mfp}$  times (rounded up) were neglected, where  $\Delta z$  is the distance from the emitter to the boundary of the biofilm on the side at which photons were collected. Tests showed that these rules had negligible effects on results.

To recreate the imaging conditions for CLSM, a 2D  $x - z$  vertical plane slicing through the center of the biofilm was imaged point-wise. This was traversed in a grid of variable resolution, where for each coordinates, a set number of photons were emitted, and were collected if their image location was within the pinhole aperture's radius  $r_0$ , where the aperture's center  $x_0, y_0$  was aligned to the emitter, so that the acceptance condition was

$$(x_d - x_0)^2 + (y_d - y_0)^2 < r_0^2 \quad (6)$$

The aperture size and collection angle (i.e. numerical aperture, NA) in the simulation



**(a)** Fraction of pixels detected when emitted from different positions within an  $x$ - $z$  slice of a biofilm, with no absorption, a scattering mean free path length of  $30\mu\text{m}$ , and 2000 photons emitted per pixel.

**(b)** Widefield simulation with a scattering length scale parameter  $40\mu\text{m}$  and no absorption. 20 photons emitted per voxel, with 10 different  $z$ -slices.

**Figure 30:** Illustrative results of optical Monte Carlo simulations.

were set equal to those used for acquisition of the CLSM validation data (1 Airy unit and 0.5, respectively). The equation for an Airy unit is

$$1 \text{ AU} = 0.61 \cdot \frac{\lambda M}{\text{NA}} \quad (7)$$

Here, no magnification  $M$  was simulated so  $M = 1$ , and the imaging wavelength  $\lambda$  was again  $530\text{nm}$ , so 1 AU is  $0.65\mu\text{m}$ .

To recreate the widefield conditions, a square CCD pixel position array was defined, and a uniform 3D grid of points projecting vertically to a concentric square with 22% additional side length (see section E.5) was ‘excited’. Each grid point emitted a fixed number of photons and if a photon’s image position struck the array, the nearest pixel had its photon count incremented.

Illustrative examples of simulations are shown in Fig 30.

## H Risk Assessment retrospective

The risk assessment submitted at the start of the year contained accurate projections of the work that would be carried out in the project. No organisms were worked with other than those mentioned. A greater-than-expected proportion of the project was spent doing computational work, but risks in this are minimal and generally avoided by taking regular breaks. The only risk that was not directly anticipated was travelling with bacterial colonies between the Engineering department and Institute for Medical Physics in order to take CLSM measurements. Standard precautions were taken for this task, such as double-sealing a secure package in which to transport them.

## References

- [1] *Biofilms: The Hypertextbook*. [Online]. Available: <https://www.hypertextbookshop.com/biofilmbook/v004/r003/> (visited on 06/01/2022).
- [2] “Public Health Image Library,” *Reference Reviews*, vol. 16, no. 8, pp. 41–41, Aug. 2002, ISSN: 0950-4125. DOI: [10.1108/rr.2002.16.8.41.411](https://doi.org/10.1108/rr.2002.16.8.41.411). [Online]. Available: <https://www.emerald.com/insight/content/doi/10.1108/rr.2002.16.8.41.411/full/html> (visited on 05/29/2022).
- [3] H.-C. Flemming and S. Wuertz, “Bacteria and archaea on Earth and their abundance in biofilms,” *Nature Reviews Microbiology*, vol. 17, no. 4, pp. 247–260, Apr. 2019, ISSN: 1740-1534. DOI: [10.1038/s41579-019-0158-9](https://doi.org/10.1038/s41579-019-0158-9). [Online]. Available: <https://www.nature.com/articles/s41579-019-0158-9> (visited on 05/15/2022).
- [4] V. Carniello, B. W. Peterson, H. C. van der Mei, and H. J. Busscher, “Physico-chemistry from initial bacterial adhesion to surface-programmed biofilm growth,” *Advances in Colloid and Interface Science*, vol. 261, pp. 1–14, Nov. 2018, ISSN: 00018686. DOI: [10.1016/j.cis.2018.10.005](https://doi.org/10.1016/j.cis.2018.10.005). [Online]. Available: <https://linkinghub.elsevier.com/retrieve/pii/S000186861830229X> (visited on 05/15/2022).
- [5] C. Berne, A. Ducret, G. G. Hardy, and Y. V. Brun, “Adhesins Involved in Attachment to Abiotic Surfaces by Gram-Negative Bacteria,” *Microbiology Spectrum*, vol. 3, no. 4, M. Ghannoum, M. Parsek, M. Whiteley, and P. Mukherjee, Eds., p. 3.4.15, Jul. 2015, ISSN: 2165-0497. DOI: [10.1128/microbiolspec.MB-0018-2015](https://doi.org/10.1128/microbiolspec.MB-0018-2015). [Online]. Available: <https://journals.asm.org/doi/10.1128/microbiolspec.MB-0018-2015> (visited on 05/15/2022).
- [6] R. M. Donlan and J. W. Costerton, “Biofilms: Survival Mechanisms of Clinically Relevant Microorganisms,” *Clinical Microbiology Reviews*, vol. 15, no. 2, pp. 167–193, Apr. 2002, ISSN: 0893-8512, 1098-6618. DOI: [10.1128/CMR.15.2.167-193.2002](https://doi.org/10.1128/CMR.15.2.167-193.2002). [Online]. Available: <https://journals.asm.org/doi/10.1128/CMR.15.2.167-193.2002> (visited on 05/15/2022).
- [7] K. Myszka and K. Czaczyk, “Characterization of Adhesive Exopolysaccharide (EPS) Produced by *Pseudomonas aeruginosa* Under Starvation Conditions,” *Current Microbiology*, vol. 58, no. 6, pp. 541–546, Jun. 2009, ISSN: 0343-8651, 1432-0991. DOI: [10.1007/s00284-009-9365-3](https://doi.org/10.1007/s00284-009-9365-3). [Online]. Available: <http://link.springer.com/10.1007/s00284-009-9365-3> (visited on 05/15/2022).
- [8] A. Karimi, D. Karig, A. Kumar, and A. M. Ardekani, “Interplay of physical mechanisms and biofilm processes: Review of microfluidic methods,” *Lab on a Chip*, vol. 15, no. 1, pp. 23–42, 2015, ISSN: 1473-0197, 1473-0189. DOI: [10.1039/C4LC01095G](https://doi.org/10.1039/C4LC01095G). [Online]. Available: <http://xlink.rsc.org/?DOI=C4LC01095G> (visited on 05/15/2022).
- [9] D. L. Wheeler, “Database resources of the National Center for Biotechnology Information,” *Nucleic Acids Research*, vol. 34, no. 90001, pp. D173–D180, Jan. 2006, ISSN: 0305-1048, 1362-4962. DOI: [10.1093/nar/gkj158](https://doi.org/10.1093/nar/gkj158). [Online]. Available: <https://academic.oup.com/nar/article-lookup/doi/10.1093/nar/gkj158> (visited on 05/15/2022).
- [10] D. Sharma, L. Misba, and A. U. Khan, “Antibiotics versus biofilm: An emerging battleground in microbial communities,” *Antimicrobial Resistance & Infection Control*, vol. 8, no. 1, p. 76, Dec. 2019, ISSN: 2047-2994. DOI: [10.1186/s13756-019-0533-3](https://doi.org/10.1186/s13756-019-0533-3). [Online]. Available: <https://aricjournal.biomedcentral.com/articles/10.1186/s13756-019-0533-3> (visited on 06/01/2022).
- [11] K. I. Wolska, A. M. Grudniak, Z. Rudnicka, and K. Markowska, “Genetic control of bacterial biofilms,” *Journal of Applied Genetics*, vol. 57, no. 2, pp. 225–238, May 2016, ISSN: 1234-1983, 2190-3883. DOI: [10.1007/s13353-015-0309-2](https://doi.org/10.1007/s13353-015-0309-2). [Online]. Available: <http://link.springer.com/10.1007/s13353-015-0309-2> (visited on 05/15/2022).
- [12] M. H. Muhammad, A. L. Idris, X. Fan, et al., “Beyond Risk: Bacterial Biofilms and Their Regulating Approaches,” *Frontiers in Microbiology*, vol. 11, 2020, ISSN: 1664-302X. [Online]. Available: <https://www.frontiersin.org/article/10.3389/fmicb.2020.00928> (visited on 05/15/2022).
- [13] S. Elias and E. Banin, “Multi-species biofilms: Living with friendly neighbors,” *FEMS Microbiology Reviews*, vol. 36, no. 5, pp. 990–1004, Sep. 2012, ISSN: 1574-6976. DOI: [10.1111/j.1574-6976.2012.00325.x](https://doi.org/10.1111/j.1574-6976.2012.00325.x). [Online]. Available: <https://academic.oup.com/femsre/article-lookup/doi/10.1111/j.1574-6976.2012.00325.x> (visited on 05/15/2022).

- [14] J. D. Bryers, “Medical biofilms,” *Biotechnology and Bioengineering*, vol. 100, no. 1, pp. 1–18, May 2008, ISSN: 00063592, 10970290. DOI: [10.1002/bit.21838](https://doi.org/10.1002/bit.21838). [Online]. Available: <https://onlinelibrary.wiley.com/doi/10.1002/bit.21838> (visited on 05/17/2022).
- [15] K. Lewis, “Persister cells and the riddle of biofilm survival,” *Biochemistry (Moscow)*, vol. 70, no. 2, pp. 267–274, Feb. 2005, ISSN: 0006-2979, 1608-3040. DOI: [10.1007/s10541-005-0111-6](https://doi.org/10.1007/s10541-005-0111-6). [Online]. Available: <http://link.springer.com/10.1007/s10541-005-0111-6> (visited on 05/17/2022).
- [16] S. Molin and T. Tolker-Nielsen, “Gene transfer occurs with enhanced efficiency in biofilms and induces enhanced stabilisation of the biofilm structure,” *Current Opinion in Biotechnology*, vol. 14, no. 3, pp. 255–261, Jun. 2003, ISSN: 09581669. DOI: [10.1016/S0958-1669\(03\)00036-3](https://doi.org/10.1016/S0958-1669(03)00036-3). [Online]. Available: <https://linkinghub.elsevier.com/retrieve/pii/S0958166903000363> (visited on 05/17/2022).
- [17] H.-C. Flemming, Ed., *Marine and industrial biofouling*, ser. Springer series on biofilms v. 4. Berlin: Springer, 2009, OCLC: ocn260209250, ISBN: 9783540697947.
- [18] S. Galié, C. García-Gutiérrez, E. M. Miguélez, C. J. Villar, and F. Lombó, “Biofilms in the Food Industry: Health Aspects and Control Methods,” *Frontiers in Microbiology*, vol. 9, p. 898, May 2018, ISSN: 1664-302X. DOI: [10.3389/fmicb.2018.00898](https://doi.org/10.3389/fmicb.2018.00898). [Online]. Available: <http://journal.frontiersin.org/article/10.3389/fmicb.2018.00898/full> (visited on 05/17/2022).
- [19] E. Ünal Turhan, Z. Erginkaya, M. Korukluoğlu, and G. Konuray, “Beneficial Biofilm Applications in Food and Agricultural Industry,” in *Health and Safety Aspects of Food Processing Technologies*, A. Malik, Z. Erginkaya, and H. Erten, Eds., Cham: Springer International Publishing, 2019, pp. 445–469, ISBN: 9783030249021. DOI: [10.1007/978-3-030-24903-8\\_15](https://doi.org/10.1007/978-3-030-24903-8_15). [Online]. Available: [https://link.springer.com/10.1007/978-3-030-24903-8\\_15](https://link.springer.com/10.1007/978-3-030-24903-8_15) (visited on 05/17/2022).
- [20] S. Satpathy, S. K. Sen, S. Pattanaik, and S. Raut, “Review on bacterial biofilm: An universal cause of contamination,” *Biocatalysis and Agricultural Biotechnology*, vol. 7, pp. 56–66, Jul. 2016, ISSN: 18788181. DOI: [10.1016/j.bcab.2016.05.002](https://doi.org/10.1016/j.bcab.2016.05.002). [Online]. Available: <https://linkinghub.elsevier.com/retrieve/pii/S1878818116300937> (visited on 05/17/2022).
- [21] R. Singh, D. Paul, and R. K. Jain, “Biofilms: Implications in bioremediation,” *Trends in Microbiology*, vol. 14, no. 9, pp. 389–397, Sep. 2006, ISSN: 0966842X. DOI: [10.1016/j.tim.2006.07.001](https://doi.org/10.1016/j.tim.2006.07.001). [Online]. Available: <https://linkinghub.elsevier.com/retrieve/pii/S0966842X06001569> (visited on 05/17/2022).
- [22] M. J. Angelaalincy, R. Navanietha Krishnaraj, G. Shakambari, B. Ashokkumar, S. Kathiresan, and P. Varalakshmi, “Biofilm Engineering Approaches for Improving the Performance of Microbial Fuel Cells and Bioelectrochemical Systems,” *Frontiers in Energy Research*, vol. 6, p. 63, Jul. 2018, ISSN: 2296-598X. DOI: [10.3389/fenrg.2018.00063](https://doi.org/10.3389/fenrg.2018.00063). [Online]. Available: <https://www.frontiersin.org/article/10.3389/fenrg.2018.00063/full> (visited on 05/29/2022).
- [23] *International Biofilm Markets and Infographics*, en-GB. [Online]. Available: <https://www.biofilms.ac.uk/international-biofilm-markets/> (visited on 05/17/2022).
- [24] W. Costerton, R. Veeh, M. Shirtliff, M. Pasmore, C. Post, and G. Ehrlich, “The application of biofilm science to the study and control of chronic bacterial infections,” *Journal of Clinical Investigation*, vol. 112, no. 10, pp. 1466–1477, Nov. 2003, ISSN: 0021-9738. DOI: [10.1172/JCI200320365](https://doi.org/10.1172/JCI200320365). [Online]. Available: <http://www.jci.org/articles/view/20365> (visited on 05/17/2022).
- [25] A. D. Verderosa, M. Totsika, and K. E. Fairfull-Smith, “Bacterial Biofilm Eradication Agents: A Current Review,” *Frontiers in Chemistry*, vol. 7, p. 824, Nov. 2019, ISSN: 2296-2646. DOI: [10.3389/fchem.2019.00824](https://doi.org/10.3389/fchem.2019.00824). [Online]. Available: <https://www.frontiersin.org/article/10.3389/fchem.2019.00824/full> (visited on 05/17/2022).
- [26] C. C. de Carvalho and M. M. R. da Fonseca, “Assessment of three-dimensional biofilm structure using an optical microscope,” *BioTechniques*, vol. 42, no. 5, pp. 616–620, May 2007, ISSN: 0736-6205, 1940-9818. DOI: [10.2144/000112403](https://doi.org/10.2144/000112403). [Online]. Available: <https://www.future-science.com/doi/10.2144/000112403> (visited on 05/20/2022).
- [27] J. S. et al., “Analysis of three-dimensional biofilms on different material surfaces,” *Biomaterials Science*, Mar. 2020.

- [28] T. J. Lambert, “FPbase: A community-editable fluorescent protein database,” *Nature Methods*, vol. 16, no. 4, pp. 277–278, Apr. 2019, ISSN: 1548-7091, 1548-7105. DOI: [10.1038/s41592-019-0352-8](https://doi.org/10.1038/s41592-019-0352-8). [Online]. Available: <http://www.nature.com/articles/s41592-019-0352-8> (visited on 05/29/2022).
- [29] *Introduction to Phase Contrast Microscopy*. [Online]. Available: <https://www.microscopyu.com/techniques/phase-contrast/introduction-to-phase-contrast-microscopy> (visited on 05/29/2022).
- [30] S. Bakshi, E. Leoncini, C. Baker, S. J. Cañas-Duarte, B. Okumus, and J. Paulsson, “Tracking bacterial lineages in complex and dynamic environments with applications for growth control and persistence,” *Nature Microbiology*, vol. 6, no. 6, pp. 783–791, Jun. 2021, ISSN: 2058-5276. DOI: [10.1038/s41564-021-00900-4](https://doi.org/10.1038/s41564-021-00900-4). [Online]. Available: <http://www.nature.com/articles/s41564-021-00900-4> (visited on 05/21/2022).
- [31] P. S. Stewart, “Diffusion in Biofilms,” *Journal of Bacteriology*, vol. 185, no. 5, pp. 1485–1491, Mar. 2003, ISSN: 0021-9193, 1098-5530. DOI: [10.1128/JB.185.5.1485-1491.2003](https://doi.org/10.1128/JB.185.5.1485-1491.2003). [Online]. Available: <https://journals.asm.org/doi/10.1128/JB.185.5.1485-1491.2003> (visited on 06/01/2022).
- [32] T. P. Robinson, J. W. T. Wimpenny, and R. G. Earnshaw, “pH gradients through colonies of *Bacillus cereus* and the surrounding agar,” *Journal of General Microbiology*, vol. 137, no. 12, pp. 2885–2889, Dec. 1991, ISSN: 0022-1287. DOI: [10.1099/00221287-137-12-2885](https://doi.org/10.1099/00221287-137-12-2885). [Online]. Available: <https://www.microbiologyresearch.org/content/journal/micro/10.1099/00221287-137-12-2885> (visited on 06/01/2022).
- [33] J. M. Christie, K. Hitomi, A. S. Arvai, et al., “Structural Tuning of the Fluorescent Protein iLOV for Improved Photostability,” *Journal of Biological Chemistry*, vol. 287, no. 26, pp. 22295–22304, Jun. 2012, ISSN: 00219258. DOI: [10.1074/jbc.M111.318881](https://doi.org/10.1074/jbc.M111.318881). [Online]. Available: <https://linkinghub.elsevier.com/retrieve/pii/S0021925820497583> (visited on 05/21/2022).
- [34] *Helber Bacteria Counting Chamber*. [Online]. Available: <https://hawksley.co.uk/products/helber-bacteria-counting-chamber> (visited on 05/30/2022).
- [35] *Digital Imaging in Optical Microscopy - Concepts in Digital Imaging - CCD Noise Sources and Signal-to-Noise Ratio — Olympus LS*. [Online]. Available: <https://www.olympus-lifescience.com/en/microscope-resource/primer/digitalimaging/concepts/ccdsnr/> (visited on 05/30/2022).
- [36] J. Schindelin, I. Arganda-Carreras, E. Frise, et al., “Fiji: An open-source platform for biological-image analysis,” en, *Nature Methods*, vol. 9, no. 7, pp. 676–682, Jul. 2012, ISSN: 1548-7091, 1548-7105. DOI: [10.1038/nmeth.2019](https://doi.org/10.1038/nmeth.2019). [Online]. Available: <http://www.nature.com/articles/nmeth.2019> (visited on 06/04/2022).
- [37] I. Arganda-Carreras, V. Kaynig, C. Rueden, et al., “Trainable Weka Segmentation: A machine learning tool for microscopy pixel classification,” *Bioinformatics*, vol. 33, no. 15, R. Murphy, Ed., pp. 2424–2426, Aug. 2017, ISSN: 1367-4803, 1460-2059. DOI: [10.1093/bioinformatics/btx180](https://doi.org/10.1093/bioinformatics/btx180). [Online]. Available: <https://academic.oup.com/bioinformatics/article/33/15/2424/3092362> (visited on 05/31/2022).
- [38] S. van der Walt, J. L. Schönberger, J. Nunez-Iglesias, et al., “Scikit-image: Image processing in Python,” *PeerJ*, vol. 2, e453, Jun. 2014, ISSN: 2167-8359. DOI: [10.7717/peerj.453](https://doi.org/10.7717/peerj.453). [Online]. Available: <https://peerj.com/articles/453> (visited on 05/31/2022).
- [39] E. Berrocal, D. L. Sedarsky, M. E. Paciaroni, I. V. Meglinski, and M. A. Linne, “Laser light scattering in turbid media Part I: Experimental and simulated results for the spatial intensity distribution,” *Optics Express*, vol. 15, no. 17, p. 10649, 2007, ISSN: 1094-4087. DOI: [10.1364/OE.15.010649](https://doi.org/10.1364/OE.15.010649). [Online]. Available: <https://opg.optica.org/oe/abstract.cfm?uri=oe-15-17-10649> (visited on 05/31/2022).
- [40] C. W. et al., “Quantitative and qualitative assessment methods for biofilm growth: A mini-review,” *Res Rev J Eng Technol*, vol. 6, Dec. 2017. [Online]. Available: <http://www.rroij.com/open-access/quantitative-and-qualitative-assessment-methods-for-biofilm-growth-a-minireview-.pdf> (visited on 06/01/2022).

- [41] R. Urniezius, A. Survyla, D. Paulauskas, V. A. Bumelis, and V. Galvanauskas, “Generic estimator of biomass concentration for *Escherichia coli* and *Saccharomyces cerevisiae* fed-batch cultures based on cumulative oxygen consumption rate,” *Microbial Cell Factories*, vol. 18, no. 1, p. 190, Dec. 2019, ISSN: 1475-2859. DOI: [10.1186/s12934-019-1241-7](https://doi.org/10.1186/s12934-019-1241-7). [Online]. Available: <https://microbialcellfactories.biomedcentral.com/articles/10.1186/s12934-019-1241-7> (visited on 06/01/2022).
- [42] M. R. Warren, H. Sun, Y. Yan, J. Cremer, B. Li, and T. Hwa, “Spatiotemporal establishment of dense bacterial colonies growing on hard agar,” *eLife*, vol. 8, e41093, Mar. 2019, ISSN: 2050-084X. DOI: [10.7554/eLife.41093](https://doi.org/10.7554/eLife.41093). [Online]. Available: <https://elifesciences.org/articles/41093> (visited on 06/01/2022).
- [43] A. H. Totten, L. Xiao, D. M. Crabb, *et al.*, “Shaken or stirred?: Comparison of methods for dispersion of *Mycoplasma pneumoniae* aggregates for persistence in vivo,” *Journal of Microbiological Methods*, vol. 132, pp. 56–62, Jan. 2017, ISSN: 01677012. DOI: [10.1016/j.mimet.2016.11.011](https://doi.org/10.1016/j.mimet.2016.11.011). [Online]. Available: <https://linkinghub.elsevier.com/retrieve/pii/S0167701216303281> (visited on 05/22/2022).
- [44] Z. Wadood, *Comparison of disaggregation procedures for enumeration and characterization of municipal sewer biofilm bacteria*, 2016. [Online]. Available: [https://www.researchgate.net/publication/314082205\\_COMPARISON\\_OF\\_DISAGGREGATION\\_PROCEDURES\\_FOR\\_ENUMERATION\\_AND\\_CHARACTERIZATION\\_OF\\_MUNICIPAL\\_SEWER\\_BIOFILM\\_BACTERIA](https://www.researchgate.net/publication/314082205_COMPARISON_OF_DISAGGREGATION_PROCEDURES_FOR_ENUMERATION_AND_CHARACTERIZATION_OF_MUNICIPAL_SEWER_BIOFILM_BACTERIA) (visited on 05/30/2022).
- [45] K. Buckingham-Meyer, L. A. Miller, A. E. Parker, *et al.*, “Harvesting and Disaggregation: An Overlooked Step in Biofilm Methods Research,” *Journal of Visualized Experiments*, no. 182, p. 62390, Apr. 2022, ISSN: 1940-087X. DOI: [10.3791/62390](https://doi.org/10.3791/62390). [Online]. Available: <https://www.jove.com/t/62390/harvesting-disaggregation-an-overlooked-step-biofilm-methods> (visited on 06/01/2022).
- [46] “M9 minimal medium (standard),” *Cold Spring Harbor Protocols*, vol. 2010, no. 8, pdb.rec12295, Aug. 2010, ISSN: 1940-3402, 1559-6095. DOI: [10.1101/pdb.rec12295](https://doi.org/10.1101/pdb.rec12295). [Online]. Available: <http://cshprotocols.cshlp.org/content/2010/8/pdb.rec12295> (visited on 06/01/2022).
- [47] *Dark Current Non-Uniformity*. [Online]. Available: [https://photonestphotos.net/GeneralTopics/Sensors\\_&\\_Raw/Dark\\_Current\\_Non-Uniformity.htm](https://photonestphotos.net/GeneralTopics/Sensors_&_Raw/Dark_Current_Non-Uniformity.htm) (visited on 05/30/2022).
- [48] J. Chalfoun, M. Majurski, T. Blattner, *et al.*, “MIST: Accurate and Scalable Microscopy Image Stitching Tool with Stage Modeling and Error Minimization,” *Scientific Reports*, vol. 7, no. 1, p. 4988, Dec. 2017, ISSN: 2045-2322. DOI: [10.1038/s41598-017-04567-y](https://doi.org/10.1038/s41598-017-04567-y). [Online]. Available: <https://www.nature.com/articles/s41598-017-04567-y> (visited on 05/22/2022).
- [49] *NetworkX — NetworkX documentation*. [Online]. Available: <https://networkx.org/> (visited on 05/30/2022).
- [50] J. S. Ploem and H. J. Tanke, *Introduction to fluorescence microscopy*, ser. Oxford science publications 10. Oxford ; New York : Oxford: Oxford University Press ; Royal Microscopical Society, 1987, ISBN: 9780198564089.
- [51] S. van de Linde, S. Aufmkolk, C. Franke, *et al.*, “Investigating Cellular Structures at the Nanoscale with Organic Fluorophores,” *Chemistry & Biology*, vol. 20, no. 1, pp. 8–18, Jan. 2013, ISSN: 10745521. DOI: [10.1016/j.chembiol.2012.11.004](https://doi.org/10.1016/j.chembiol.2012.11.004). [Online]. Available: <https://linkinghub.elsevier.com/retrieve/pii/S1074552112004280> (visited on 05/18/2022).
- [52] *Microscope Calculations: Field of View, Depth of Field, Numerical Aperture*, en-US. [Online]. Available: <https://dovermotion.com/applications-capabilities-automated-imaging/microscope-calculations/> (visited on 05/30/2022).
- [53] A. Nwaneshiudu, C. Kuschal, F. H. Sakamoto, R. Rox Anderson, K. Schwarzenberger, and R. C. Young, “Introduction to Confocal Microscopy,” *Journal of Investigative Dermatology*, vol. 132, no. 12, pp. 1–5, Dec. 2012, ISSN: 0022202X. DOI: [10.1038/jid.2012.429](https://doi.org/10.1038/jid.2012.429). [Online]. Available: <https://linkinghub.elsevier.com/retrieve/pii/S0022202X15355536> (visited on 05/30/2022).
- [54] *The Henyey-Greenstein Phase Function : Ocean Optics Web Book*. [Online]. Available: <https://www.oceanopticsbook.info/view/scattering/level-2/the-henyey-greenstein-phase-function> (visited on 06/01/2022).